A synthetic synaptic organizer protein restores glutamatergic neuronal circuits

Kunimichi Suzuki[1,9,†], Jonathan Elegheert[2,10,†], Inseon Song[3,†], Hiroyuki Sasakura[4,†], Oleg Senkov[3], Keiko Matsuda[1], Wataru Kakegawa[1], Amber J. Clayton[2,11], Veronica T. Chang[2,5], Maura Ferrer-Ferrer[3], Eriko Miura[1], Rahul Kaushik[3,7], Masashi Ikeno[4], Yuki Morioka[4], Yuka Takeuchi[4], Tatsuya Shimada[1], Shintaro Otsuka[1], Stoyan Stoyanov[3], Masahiko Watanabe[8], Kosei Takeuchi[4], Alexander Dityatev[3,6,7,*], A. Radu Aricescu[2,5,*], Michisuke Yuzaki[1,*]

[1]Department of Physiology, Keio University School of Medicine, Tokyo 160-8582, Japan

[2]Division of Structural Biology, University of Oxford, Oxford OX3 7BN, UK

[3]Molecular Neuroplasticity, German Center for Neurodegenerative Diseases (DZNE), 39120 Magdeburg, Germany

[4]Department of Medical Cell Biology, School of Medicine, Aichi Medical University, Aichi, Japan

[5]Neurobiology Division, MRC Laboratory of Molecular Biology, Cambridge CB2 0QH, UK

[6]Medical Faculty, Otto-von-Guericke-University, 39120 Magdeburg, Germany

[7]Center for Behavioral Brain Sciences (CBBS), 39106 Magdeburg, Germany

[8]Department of Anatomy, Hokkaido University Graduate School of Medicine, Sapporo 060-8638, Japan

Abstract

Neuronal synapses undergo structural and functional changes throughout life, which are essential for nervous system physiology. However, these changes may also perturb the excitatory/inhibitory neurotransmission balance and trigger neuropsychiatric and neurological disorders. Molecular tools to restore this balance are highly desirable. Here, we designed and characterized CPTX, a

[*]Corresponding author. alexander.dityatev@dzne.de (A.D.); radu@mrc-lmb.cam.ac.uk (A.R.A.); myuzaki@keio.jp (M.Y.).
[9]Present address: Neurobiology Division, MRC Laboratory of Molecular Biology, Cambridge CB2 0QH, UK
[10]Present address: Interdisciplinary Institute for Neuroscience (IINS), UMR5297 CNRS/UB, 33076 Bordeaux, France.
[11]Present address: Adaptimmune, 60 Jubilee Avenue, Milton Park, Abingdon OX14 4RX, UK.
[†]Co-first authors.

synthetic synaptic organizer combining structural elements from cerebellin-1 and neuronal pentraxin-1. CPTX can interact with presynaptic neurexins and postsynaptic AMPA-type ionotropic glutamate receptors and induced the formation of excitatory synapses both in vitro and in vivo. CPTX restored synaptic functions, motor coordination, spatial and contextual memories, and locomotion in mouse models for cerebellar ataxia, Alzheimer's disease and spinal cord injury, respectively. Thus, CPTX represents a prototype for structure-guided biologics that can efficiently repair or remodel neuronal circuits.

A broad range of neuropsychiatric and neurological disorders, including autism spectrum disorders, epilepsy, schizophrenia and Alzheimer's disease, are thought to be caused by an imbalance between excitatory and inhibitory (E/I) synaptic functions (1–5). During organism development, but also throughout life, the formation and remodeling of complex yet precise neuronal circuits rely on specific synaptic organizing proteins (6, 7). These include cell adhesion molecules, such as neurexins (Nrxs), neuroligins (8, 9) and receptor protein tyrosine phosphatases (10), as well as secreted proteins, such as fibroblast growth factors, semaphorins, Wnt and extracellular scaffolding proteins (ESPs) (7, 11, 12). ESPs directly connect pre- and postsynaptic membrane proteins to form molecular bridges that span the synaptic cleft and mediate bidirectional signaling. For example, cerebellin-1 (Cbln1) is released from parallel fibers (PFs; axons of cerebellar granule cells) and contributes to the synapse-spanning tripartite complex Nrx–Cbln1– GluD2 (the ionotropic glutamate receptor family member delta-2) (Fig. 1A, left panel). Cbln1 can simultaneously bind Nrx isoforms containing the 30-residue "spliced sequence 4" (SS4) insert (Nrx(+4)) expressed at PF terminals and the amino-terminal domains (ATD) of GluD2 on Purkinje cells (PCs) (13–15). Importantly, a single injection of recombinant Cbln1 into the cerebellum can restore ~75% PF–PC synapses and normal motor coordination within 1 d in adult *Cbln1*-null mice in vivo (16). Cerebellins (Cbln1–4) are expressed in nearly all brain regions with distinct patterns and developmental dynamics (17, 18). Cbln1 promotes the formation or maintenance of excitatory synapses in the nucleus accumbens (19), while Cbln2 is necessary for excitatory synapses in the interpeduncular nucleus (20) and the hippocampus (21, 22). Cbln4 mediates the formation of inhibitory synapses between pyramidal neurons and cortical interneurons (23) by interacting postsynaptically with GluD1 (24), a receptor closely related to GluD2 (25). Other ESPs, such as the C1q-related C1ql1, promote excitatory synapse formation and maintenance in the cerebellum by binding to the adhesion G-protein coupled receptor BAI3 (26, 27). C1ql3 also mediates synapse formation and maintenance in the medial prefrontal cortex (28). C1ql2 and C1ql3 are produced by mossy fibers and recruit kainate-subtype ionotropic glutamate receptors (KARs) by directly binding to the ATDs of GluK2/4 KAR subunits in CA3 hippocampal neurons (29, 30). Molecular components of excitatory synapses are considerably different among neuronal circuits (31, 32) and other ESPs likely remain to be discovered. Nevertheless, the Cbln1– Cbln4 and C1ql1–C1ql3 examples prompted us to hypothesize that synthetic molecules with defined pre- and post-synaptic binding specificities could be designed and employed to reverse the loss of synapses and promote the structural and functional recovery of damaged neuronal circuits.

Design of a synthetic ESP-type synaptic organizer

Neuronal pentraxins (NPs) are a family of oligomeric secreted (NP1 and NP2) or membrane-attached (NPR) proteins that induce clustering of postsynaptic AMPA-type ionotropic glutamate receptors (AMPARs) through direct interactions between pentraxin (PTX) domains and the AMPAR ATDs (33–36). Astrocyte-secreted glypican 4 indirectly leads to AMPAR recruitment by enhancing the release of NP1 from pre-synaptic axons (37). However, unlike Cbln1 (13, 16) and Cbln4 (23, 24), NPs do not seem to induce presynaptic specializations in vivo (38, 39) (Fig. 1A, middle panel). Thus, we hypothesized that we could exploit the modular architecture of NP1 and Cbln1 to develop a synthetic hexameric ESP, termed CPTX, which would include the N-terminal cysteine-rich region (CRR) of Cbln1 that binds Nrx(+4) and the PTX domain of NP1 (Fig. 1A, right panel). CPTX should have the potential to induce the formation of excitatory synapses by organizing Nrx nanoclusters (40) and to form a trans-synaptic complex by recruiting postsynaptic AMPARs (41).

To define the correct domain boundaries for CPTX assembly, we first solved the crystal structure of the PTX domain of NP1 (NP1$_{PTX}$) at 1.45 Å resolution (Fig. 1B and Table S1). Reminiscent of short pentraxins (42), such as the C-reactive protein and serum amyloid P component, NP1$_{PTX}$ formed a two-layered β sheet with a flattened jellyroll topology containing two Ca^{2+} ions (Fig. 1B and fig. S1). However, unlike short pentraxins, NP1$_{PTX}$ is monomeric in the crystal as well as in solution, as confirmed by multi-angle light scattering (MALS; Fig. 1C). Surface plasmon resonance (SPR) assays, performed to identify the minimal domain requirements for NP1–GluA interactions, revealed that NP1$_{PTX}$ bound the ATDs of GluA1, GluA3 and GluA4 AMPARs with affinities in the high μM range (Fig. 1D). A recent analysis of the Nrx–Cbln1– GluD2 trans-synaptic complex showed a similarly weak interaction between the globular domain of Cbln1 and the GluD2 ATD; however, avidity effects arising from the oligomeric nature of Cbln1 (hexamer) and GluD2 (tetramer) increase the apparent affinity between the full-length partners considerably (15). To mimic the structural organization of Cbln1 in CPTX, we first added a triple-coil-forming mutant GCN4 peptide to the amino-terminus of NP1$_{PTX}$, resulting in the NP1$_{PTX-3Cl}$ construct, and confirmed its trimeric stoichiometry (Fig. 1C). The Cbln1 CRR (15) was then added to the NP1$_{PTX-3Cl}$ N-terminus, leading to the hexameric CPTX molecule (Fig. 1C and fig. S1).

We next examined whether CPTX was equipped with the intended dual binding capacity in vitro. SPR assays showed that CPTX and NP1$_{PTX}$ bound the ATD of GluA4 with comparable apparent affinities (K_D 4.5 ± 0.5 μM and 11.0 ± 0.9 μM, respectively; Fig. 1D and fig. S2). Like NP1$_{PTX}$, CPTX also bound to the other GluA ATDs with a GluA3 > GluA1 > GluA2 preference. However, these interactions were weaker and accurate K_D values could not be determined reliably (Fig. 1D and fig. S2). In addition, CPTX bound specifically to the Nrx1β(+4) ectodomain (K_D 4.9 ± 0.9 nM), but not Nrx1β(–4) (Fig. 1E), thus retaining the strict isoform recognition specificity of Cbln1. Cell-based binding assays also showed that CPTX bound specifically to human embryonic kidney (HEK) cells displaying GluA1–GluA4 ATDs on their surface, while Cbln1 only bound those displaying the GluD2 ATD (fig. S3A). On the other hand, both Cbln1 and CPTX bound to HEK293 cells expressing full-length Nrx1α, Nrx1β, Nrx2β, and Nrx3β only when the SS4 insert was

present (fig. S3B). The ectodomain of Nrx1β(+4) specifically bound to HEK293 cells expressing GluA4 ATD under CPTX application (fig. S3C). Thus, CPTX can simultaneously bind GluAs and neurexin isoforms containing the SS4 insert.

CPTX induces excitatory pre- and postsynaptic sites in vitro

We examined whether CPTX could serve as a synaptic organizer with the designed GluA vs. GluD specificity in neuronal cell cultures. Application of CPTX to *Cbln1*-null cerebellar granule cells induced punctate accumulation of endogenous synaptophysin, a synaptic vesicle marker, in axons that contact HEK293 cells displaying GluA ATDs on their surface, but not in those that contact cells displaying the GluD2 ATD (Fig. 2A and fig. S4A). Similarly, CPTX induced accumulation of synaptophysin (fig. S4B) or vesicular glutamate transporter 1 (VGluT1) (fig. S4C) in wild-type hippocampal neurons that contacted HEK293 cells displaying GluA ATDs. In contrast, NP1 could bind to the surface of HEK293 cells displaying the GluA4 ATD but failed to accumulate synaptophysin (fig. S4D). Conversely, application of Cbln1 induced presynaptic synaptophysin accumulation in axons that contact co-cultured HEK293 cells expressing GluD2, but not GluA ATDs (Fig. 2A and fig. S4A, B). To examine the direct effect of CPTX, we applied beads coated with CPTX to hippocampal neurons in culture. Cbln1- or CPTX-coated beads accumulated presynaptic sites positive for endogenous synaptophysin, Nrx and VGluT1 (Fig. 2B and fig. S5A– B), indicating that CPTX can directly induce presynapses in vitro.

We further asked whether CPTX could induce postsynaptic sites in vitro. Co-expression of Nrx1β(+4) and CPTX, but not Cbln1, on the surface of HEK293 cells facilitated accumulation of endogenous GluA1–3 in dendrites of contacted hippocampal neurons (fig. S6A). Similarly, beads coated with CPTX, but not Cbln1, accumulated endogenous GluA1– GluA3 in dendrites of most hippocampal neurons (Fig. 2B and fig. S6B) and GluA4 in parvalbumin-positive (PV[+]) interneurons (fig. S6C). Immunocytochemical analyses revealed that soluble CPTX added to the culture medium accumulated between Homer- and Bassoon-positive puncta (fig. S7A) and at puncta double immunopositive for GluA1–4 and Nrx or VGluT1 (Fig. 2C and fig. S7B). CPTX also increased Nrx and GluA intensities in GluA/ Nrx- and GluA/VGluT1-double immunopositive areas, respectively. Thus, CPTX serves as a bidirectional synaptic organizer by binding presynaptic Nrx(+4) and postsynaptic AMPARs in vitro.

Rescue of synapse formation and motor coordination by CPTX in cerebellar ataxia mice

To test the impact of CPTX in vivo, we injected it into the cerebellum (lobules VI and VII) of adult *Cbln1*-null mice. Immunohistochemical analyses 1 d after the injection showed that CPTX was preferentially confined to the injected molecular layer (fig. S8A) and co-localized with VGluT1 (a PF terminal marker), but not VGluT2 (a climbing fiber terminal marker) or the vesicular GABA transporter (VGAT, a marker for inhibitory inputs) (fig. S8B). Thus, CPTX was mainly located along PC dendrites where PFs that specifically express Nrx(+4) (43) make synapses. Electron microscopy analysis revealed that single injections of CPTX partially restored PF–PC synapses in *Cbln1*-null mice (fig. S8C). The

effect was weaker than for Cbln1 (13, 16), probably because there is a large excess of GluD2 relative to GluAs at PF–PC synapses (44). Whole-cell patch-clamp recordings in acute slice preparations showed that CPTX, but not NP1$_{PTX-3Cl}$, increased the amplitudes of PF-evoked excitatory postsynaptic currents (PF-EPSCs) (fig. S8D). Thus, CPTX most likely regulates synaptic functions by bridging pre- and postsynaptic sites. Furthermore, CPTX was as effective as Cbln1 in restoring normal gait patterns (fig. S8E and fig. S9A; Movie S1 and Movie S2). We also observed recovery of motor coordination as measured by the rotor-rod test in the ICR mouse genetic background (fig. S9B), but not in the C57BL/6 one where the loss of the skilled motor coordination phenotype was too severe. Similar to Cbln1 (16), the effect of CPTX on the rotor-rod performance recovery was maximal at 3 d post-injection but decayed afterward (fig. S9C), suggesting that continued presence of CPTX is necessary to maintain PF–PC synapses in the longer term. Thus, CPTX can induce functional PF–PC synapses that contribute to the restoration of the motor phenotypes in adult *Cbln1*-null mice.

We next investigated whether CPTX could serve as a synaptic organizer in the absence of GluD2 in vivo. As observed in *Cbln1*-null mice, injected CPTX was localized at PF–PC synapses in *GluD2*-null mice (Fig. 3A–B). Although Cbln1 and GluD2 form a trans-synaptic complex, *GluD2*-null mice are reported to show more severe motor phenotypes with less reduced PF–PC synapses (~40–60% of wild-type) than *Cbln1*-null mice (~20–30%) (13, 16). While Cbln1 was completely ineffective in *GluD2*-null mice in restoring morphological (Fig. 3C) and functional (Fig. 3D) PF–PC synapses, CPTX partially restored these phenotypes. CPTX, but not Cbln1, reset the increased paired-pulse ratio (PPR) of PF-EPSCs to wild-type levels (16) (Fig. 3D). Furthermore, unlike Cbln1, CPTX improved the gait of *GluD2*-null mice (Fig. 3E and Movie S3). Thus, CPTX can induce PF–PC synapses that contribute to cerebellar functions independent of GluD2 in vivo.

CPTX induces synaptic AMPAR accumulation in the wild-type hippocampus

To test if CPTX could act in brain regions outside the cerebellum, we injected CPTX into the dorsal hippocampus of Thy1-GFP and wild-type mice. Injected CPTX diffused throughout the entire CA1 regions of dorsal hippocampi and was detected between Bassoon-positive presynaptic terminals and GFP-positive postsynaptic sites of the CA1 pyramidal neurons in Thy1-GFP mice at 3 d after injection (fig. S10A). Super-resolution microscopy revealed that CPTX was localized between VGluT1 and AMPAR puncta in the CA1 *stratum radiatum* at 1 d after injection (fig. S10B, C). In contrast, CPTX did not show any co-localization with inhibitory synaptic markers (fig. S11). Immunohistochemistry of CPTX and each AMPAR subunit (fig. S12A) revealed that CPTX shifted the intensity histogram of GluA1 to higher values, while causing redistribution of GluA2/3 signals among puncta (fig. S12B–D). As a result, CPTX increased the size of high-intensity (> mean + 3 SD) puncta of GluA1 and GluA2/3 (fig. S12E, F). In contrast, while CPTX also shifted the intensity histogram of GluA4 to higher values (fig. S12D), it did not affect the size of high-intensity GluA4 puncta (fig. S12F). Thus, CPTX selectively binds to excitatory synapses in the hippocampus and modifies the distribution of AMPARs in a subunit-dependent manner.

Functionally, the CPTX injection increased the frequency of miniature EPSCs (mEPSCs) in CA1 pyramidal neurons as early as 4 h after application to acute hippocampal slices (fig.

S13A). CPTX also upregulated both the amplitude and frequency of mEPSCs in hippocampal slices prepared 3 d after injection (fig. S13B) but did not enhance the frequency and amplitude of mEPSCs in CA1 PV+ interneurons (fig. S14), which express high levels of GluA4 and NP1/NPR (fig. S15 and fig. S16A, B, E). In the CA1 *lacunosum moleculare* where NP1/NPR immunoreactivities were much weaker (fig. S16C), CPTX injections showed stronger effects in increasing the GluA1–3 intensity (fig. S17) than in the *stratum radiatum* (fig. S12). Thus, the impact of CPTX depends on the endogenous levels of NPs: in CA1 PV+ interneurons, the ATD of GluA4, where CPTX binds, would most likely be occupied by endogenous NPs while in other regions, where NPs are less abundant, CPTX appears more likely to bind and cluster GluAs.

CPTX restores spines, LTP and cognition in an Alzheimer's disease model

Prompted by these observations, we next examined whether CPTX could modify neuronal circuits in the hippocampus under pathological conditions in vivo. We used 5xFAD mice, a model of early familial Alzheimer's disease (AD), which allowed us to test the impact of CPTX in the context of severe loss of neurons, synapses, synaptic plasticity, and cognitive abilities (45, 46). We focused on Schaffer collateral (SC)–CA1 synapses, which are most relevant to contextual fear conditioning. Golgi staining showed that the reduced spine densities in 5xFAD mice (11–12 months old) were restored by injection of CPTX into the hippocampus of 5xFAD mice (Fig. 4A and Movie S4). We next immunostained PSD95, the key excitatory synaptic scaffold protein required for synaptic stabilization, together with synaptophysin, GluA1–3 and GluN1, an essential NMDA receptor subunit in the hippocampus (fig. S18A). CPTX caused the redistribution of PSD95 as well as GluA1–3 signal intensities without affecting synaptophysin or GluN1 signals (fig. S18B, C). CPTX also increased the proportion of large puncta positive for PSD95 and GluA1–3, but not GluN1 or synaptophysin (fig. S18D). Extracellular field recordings confirmed that excitatory postsynaptic potentials (fEPSPs) induced by SC stimulation were reduced in acute slices prepared from 5xFAD mice (Fig. 4B) as reported earlier (47). CPTX restored the amplitude of SC-fEPSPs, which became even larger than in the wild-type hippocampus (Fig. 4B). In contrast, NP1$_{PTX-3Cl}$ failed to increase SC-fEPSPs (fig. S19), a result consistent with the lack of effect of NP1 in inducing synapses in vitro (fig. S4D). CPTX did not affect the PPR of SC-fEPSPs, probably because the PPR was normal in 5xFAD hippocampus (Fig. 4C), a phenotype different from *GluD2*-null cerebellum (Fig. 3D). Moreover, whole-cell patch-clamp recordings from CA1 pyramidal neurons revealed that the frequency and the amplitude of mEPSCs were increased in 5xFAD mice injected with CPTX (Fig. 4D). On the other hand, miniature inhibitory synaptic currents (mIPSCs) were unaffected (Fig. 4D). Thus, CPTX specifically improved excitatory transmission between principal cells without changing GABAergic transmission in 5xFAD mice.

Impaired long-term potentiation at SC-CA1 synapses (SC-LTP) is believed to underlie certain cognitive abnormalities in 5xFAD mice (47). Interestingly, CPTX injection rescued impaired SC-LTP in middle-aged 5xFAD mice (Fig. 4E). Because CPTX did not increase GluN1 immunoreactivities, it is plausible that newly formed spines (Fig. 4A) and redistribution of PSD95 and AMPARs (fig. S18) may contribute to restoration of LTP. To evaluate spatial memory in a paradigm with minimal stress exposure, we placed three groups

of mice in a labyrinth with food pellets as a reward and measured the total distance that mice traveled to reach the goal during the encoding and retrieval sessions (Fig. 5A). Although there was no difference in the travel distance between each group during the encoding session, 5xFAD mice traveled longer distances than wild-type mice during the retrieval session. CPTX injection 3 d before the learning test decreased the distance that 5xFAD mice traveled in the retrieval session, suggesting an improvement of spatial learning after the CPTX treatment. After reversal learning, when mice had to find a reward in a new position, the performance of 5xFAD mice was impaired in the mock-, but not in CPTX-injected group, as compared to wild-type mice (Fig. 5A). The modest effect of CPTX in this test may be caused by the insufficient spread of CPTX because spatial memory requires integration of information from head direction cells, grid cells and place cells with landmarks (context). To more directly assess the function of the CA1 region, we next evaluated contextual fear conditioning by exposing the same three groups of mice to an electrical shock in context A and measuring the freezing time in the conditioned context A and a neutral context B 1 d later. 5xFAD mice failed to discriminate context A from B, i.e. showed generalized rather than context-specific learned fear responses. CPTX injection 5 d before fear conditioning improved context discrimination in 5xFAD mice to be even better than in mock-treated wild-type controls (Fig. 5B), indicating that CPTX could rescue the context generalization in 5xFAD mice. Thus, CPTX injection rescues the impaired basal excitatory transmission, SC-LTP and hippocampus-dependent learning in middle-aged 5xFAD mice.

CPTX restores synapses and locomotion in spinal cord injury models

Re-organization and the E/I balance of spared intra-spinal networks have recently been shown to contribute to functional recovery after spinal cord injury (SCI) (48, 49). To test whether CPTX could restore glutamatergic circuits in the spinal cord, we performed dorsal hemisections at the thoracic vertebra 10 (T10) in mice and injected CPTX rostral to the injured region (Fig. 6A). Spinal cords were dissected 2–5 d after injections and coronal serial sections were immunostained for VGluT2 and CPTX (fig. S20A). CPTX was distributed in the gray matter and was largely colocalized with VGluT2 and GluA4 immunopositive (VGluT2+ and GluA4+) puncta in a region 1.4–1.6 mm rostral to the epicenter of the injured site (fig. S20A–C). Super-resolution microscopy revealed that CPTX was located between VGluT2+ and GluA4+ puncta (Fig. 6B). Most excitatory spinal cord interneurons that are involved in locomotion express high levels of VGluT2, GluA4 (50) and Nrx(+4) (51). In contrast, NP1/NPR immunoreactivities were very weak in most of the spinal cord (fig. S16D, E), indicating that the ATDs of GluA4 are not occupied by endogenous NPs. Thus, CPTX may connect excitatory pre- and postsynaptic sites of spared neuronal circuits.

We next assessed whether CPTX induced excitatory synapses by quantifying the intensity and the size of VGluT2+, GluA4+ and CPTX+ puncta (Fig. 6C). CPTX signal was higher at GluA4+/VGluT2+-double-positive puncta than at single GluA4+ or VGluT2+ puncta, suggesting preferential localization of CPTX at synapses (fig. S20D). Furthermore, CPTX increased the percentage of VGluT2+ puncta that were also GluA4+ (Fig. 6D). Thus, CPTX induced GluA4+ excitatory synapses within regions spared by the injury (fig. S20A, B).

Finally, we assessed the recovery of locomotion after spinal cord hemisections. For comparison, we separately injected chondroitinase ABC (ChABC), an enzyme that promotes robust nerve regeneration (52), as well as Cbln1 to the lesioned spinal cord. During the acute stage, single injections of CPTX as well as ChABC, but not Cbln1, significantly restored the Basso Mouse Scale (BMS) score (53) (Fig. 6E and Movie S5) and other locomotive parameters examined until 6 weeks after the injury (fig. S21A and Movie S6). ChABC delivered 1 week after the hemisection was less effective (Fig. 6F), as reported previously (54). In contrast, when CPTX was delivered 1 week after injury it was most effective (Fig. 6F and fig. S21B; Movie S7 and Movie S8). CPTX also efficiently restored locomotion in a contusion SCI model, which is considered closer to pathophysiology that occurs commonly in humans (Fig. 6G and fig. S21C). In this paradigm, a combination of CPTX and ChABC treatment showed the most prominent recovery of locomotion, especially in the early stages after contusion. Immunoblot analyses revealed that by 7 d after injection, CPTX became undetectable in the spinal cord as well as in the hippocampus and the cerebellum (fig. S22). Thus, CPTX may directly enhance excitatory connectivity, which may be further stabilized by endogenous synaptic organizers, to promote sustained functional recovery in spinal cord injury models. Mechanistically, this process appears to be distinct from the one induced by ChABC treatment.

Discussion

Here, we developed a synthetic, structure-guided, synaptic organizer termed CPTX that is able to induce functional and structural synapses in the cerebellar, hippocampal and spinal cord neuronal circuits in vivo. CPTX induced accumulation of AMPARs, as revealed by increased GluA1 intensity in all puncta and redistribution of GluA2/3 signals in the hippocampus 1 d after injection. CPTX application to the wild-type hippocampus led to increased mEPSCs frequency in ~4 h, and then both the frequency and the amplitude of mEPSCs ~3 d later. Thus, we speculate that CPTX first accumulates pre-existing surface AMPARs at immature synapses with loose perisynaptic extracellular matrix (55), leading to redistribution of AMPARs and the increased mEPSC frequency. Considering that GluA1-containing AMPARs traffic to the surface in an activity-dependent manner (56), CPTX may stabilize newly inserted GluA1-containing AMPARs in mature synapses leading to increased GluA1 surface levels and mEPSC amplitudes. Interestingly, NP1 or NP1$_{PTX-3Cl}$, which could bind to AMPARs, failed to induce excitatory synapses in the hippocampus. Moreover, NP1$_{PTX-3Cl}$ could not restore PF-EPSCs in *Cbln1*-null mice. Thus, we propose that CPTX induces functional synapses by connecting pre-synaptic neurexin with post-synaptic AMPARs and facilitating trans-synaptic alignment of AMPARs with the synaptic vesicle release sites. Such "molecular bridges" may initiate presynaptic maturation by inducing Nrx nanoclusters (40) and may eventually integrate within trans-synaptic nanocolumns at excitatory synapses (41). Because molecular components are considerably different among neuronal synapse types and circuits, further studies are warranted to test this hypothesis and clarify the detailed molecular mechanisms by which CPTX restores functional and structural excitatory synapses under pathological conditions.

Potential adverse effects of CPTX could include inhibition of synapses where CPTX binds GluAs but does not have a presynaptic Nrx(+4) partner. However, injected CPTX did not

replace endogenous NPs that target the ATD of GluA4. CPTX could also cause artificial hyper-connectivity, but we did not notice obvious abnormal behaviors, such as seizures or hyperactivities, in mice injected with CPTX into the hippocampus, the spinal cord or the cerebellum. Most likely this is because CPTX selectively strengthens synapses that contain Nrx(+4) at presynaptic sites. However, constitutive expression of Nrx3(+4) in genetically modified mice reduces mEPSC frequency and decreases LTP (51). Thus, the dose and the affinity of CPTX-like molecules should be optimized for future therapeutic use.

Novel ESPs continue to be discovered. For example, LGI1, an ESP produced by the hippocampal neurons, is particularly interesting because it indirectly recruits AMPARs by binding to pre- and postsynaptic ADAM23 and ADAM22, respectively (57, 58). Owing to their modular structure, we anticipate that the toolkit of synthetic ESPs can be expanded to include a variety of pre- and postsynaptic specificities, with a range of affinities and enhanced resistance to proteolytic degradation in vivo. Such ESPs could be used to restore or modify synaptic connectivity in various neuronal circuits. The structure-guided design of ESPs that target specific $GABA_A$ receptor subtypes (59), as well as specific AMPAR or KAR subunits, will be useful to restore E/I balance in specific neuronal circuits affected by autism spectrum disorders and schizophrenia (1, 5, 60), epilepsy (3) and Alzheimer's disease (2). Importantly, while the effect of CPTX was transient in *Cbln1*-null ataxia mice, a single injection of CPTX greatly enhanced locomotion for at least 7–8 weeks in SCI models, long after injected CPTX was degraded. In the cerebellum, PF-PC synapses rely heavily on Cbln1 and GluD2 as synaptic organizers. Thus, once the injected CPTX is degraded, cerebellar synapses are rapidly lost and ataxic phenotypes return quickly. In contrast, in 5xFAD mice and SCI models, the new synapses formed upon CPTX injection might survive longer because other (endogenous) synaptic organizers could be recruited by increased neuronal activities. Thus, synthetic ESPs built upon the principles described here may become powerful tools to investigate and potentially cure disorders associated with impaired neuronal connectivity.

Materials and Methods

Mice

Wild-type (Charles River Laboratories and Japan SLC) and *Cbln1*-null mice were used for primary culture. In experiments assessing cerebellar functions, we used male and female *Cbln1*-null mice with the C57BL/6J or ICR genetic backgrounds and *GluD2*-null mice (13) with the C57BL/6J genetic background. They were housed on a conventional 12 h light/dark cycle (light on at 8:30 a.m.) and their behavior was tested in the light phase of the cycle. Mice expressing enhanced green fluorescent protein (EGFP) under the control of a modified Thy1 promoter region (The Jackson Laboratory, cat. # 007788) were used for immunocytochemistry. In experiments assessing hippocampal functions, we used male C57BL/6J, PV-*Cre*/Ai9 double transgenic mice (The Jackson Laboratory, cat. # 017320 and 007909), 5xFAD mice (The Jackson Laboratory, cat. # 006554) which carry 5 familial Alzheimer's disease mutations, and their wild-type littermates with C57BL/6J genetic background (Charles River Laboratories). At least one week before starting the experiments, mice were transferred from the main animal facility of DZNE (Magdeburg, Germany) to a

small vivarium, where they were housed individually with food and water *ad libitum* before food restriction diet (FRD) was given, on a reversed 12 h light/dark cycle (light on at 9:00 p.m.). All behavioral experiments assessing hippocampal functions were performed in the late afternoons during the dark phase of the cycle when mice were active, under constant temperature (22 ± 1°C) and humidity ($55 \pm 5\%$). For the spinal cord injury (SCI) model, wild-type mice with the ICR genetic background (Japan SLC) were used. They were housed on a conventional 12 h light/dark cycle. Locomotor functions were assessed at a fixed time in the evening. All treatments and behavioral procedures were conducted in accordance with ethical animal research standards defined by German and Japanese law and approved by the Ethical Committee on Animal Health and Care of the State of Saxony-Anhalt, Germany, with license numbers 42502-2-1343 DZNE and 42502-2-1322 DZNE, by the Animal Resource Committee of Keio University (No. 09050) and by the Institutional Animal Care and Use Committee of Aichi Medical University (No. 1559).

Plasmids

For surface plasmon resonance (SPR) experiments, cDNAs encoding the extracellular human glutamate receptor D2 amino-terminal domain (ATD; UniProt ID O43424; GluD2 ATD: Asp24-Gly440), the mouse glutamate receptor A1 ATD (UniProt ID P23818; GluA1 ATD: Ala19-Thr412), the mouse glutamate receptor A2 ATD (UniProt ID P23819; GluA2 ATD: Val22-Thr419), the mouse glutamate receptor A3 ATD (UniProt ID Q9Z2W9; GluA3 ATD: Gly23-Thr422), the mouse glutamate receptor A4 ATD (UniProt ID Q9Z2W8; GluA4 ATD: Gly21-Thr420), the human β-neurexin-1 LNS6 domain including sliced sequence #4 (UniProt ID P58400; β-Nrx1 LNS6(+SS4): His86-Val295) and the pentraxin domain of human neuronal pentraxin-1 (UniProt ID Q15818; $NP1_{PTX}$: Pro224-Ile431) were cloned into the pHLsec-Avitag3 expression vector (Addgene cat. # 99847) (61). To produce a trimeric form of the pentraxin domain, $NP1_{PTX}$ was fused to the C-terminus of a three-stranded GCN4 leucine zipper coiled-coil sequence (62) to yield $NP1_{PTX-3Cl}$ (fig. S1A-B). To produce CPTX, $NP1_{PTX-3Cl}$ was fused to the C-terminus of the cysteine-rich region (CRR) (15) of human Cbln1 (UniProt ID P23435; Gln22-Ile53) (fig. S1A-B). For the *in vitro* binding and synapse formation assays, cDNA encoding the (i) full-length mouse NP1 (UniProt ID Q62443) was cloned into the pCAGGS vector (a gift from Dr. J. Miyazaki, Osaka University, Osaka, Japan) with a C-terminal HA-tag (fig. S4D), (ii) full-length mouse β-Nrx1 (UniProt ID P0DI97; ±SS4 −SS5), full-length rat β-Nrx2 (UniProt ID Q63376; ±SS4 −SS5) with the signal sequence of mouse neuroligin-1 (UniProt ID Q99K10; Met1-Lys47), full-length mouse β-Nrx3 (UniProt ID Q8C985; ±SS4 +SS5), and full-length rat α-Nrx1 (UniProt ID Q63372; − SS1,2,4,6 +SS3,5 or −SS1,2,5,6 +SS3,4; a gift from Dr. P. Scheiffele, University of Basel, Switzerland) was cloned into pCAGGS with a C-terminal FLAG-tag (fig. S3B and fig. S6A), (iii) mouse β-Nrx1 extracellular domain (UniProt ID P0DI97; Met1-Thr392, +SS4 −SS5) was cloned into the pCAGGS vector with a C-terminal human Fc tag (fig. S3C), and (iv) Myc-tagged GluA1–4 ATDs were cloned into a modified pDisplay vector (Invitrogen) as described previously (29) (fig. S3A, C and fig. S4A-D). The 21-nt miR RNAi sequences targeting mouse *Nptx1* and *Nptxr* mRNA were designed by BLOCK-iT (Invitrogen) and inserted upstream of IRES-GFP in the pCAGGS vector as described previously (64) (sequences: 5'-AGA CAA GTT TCA GCT GAC ATT-3' for NP1 and 5'-TGC TCA GTC GCT TCC TCT GTA-3' for NPR). For immunocytochemical

analyses to check the selectivity of anti-NP1 and anti-NPR antibodies (fig. S15C-D), full-length mouse NP1 (UniProt ID Q62443), full-length mouse NP2 (GenBank ID O70340) and full-length mouse NPR (UniProt ID Q99J85) were cloned into the pCAGGS vector with a C-terminal HA-tag. For the immunoblotting analyses to check the selectivity of anti-NP1 and anti-NPR antibodies (fig. S15A-B), mouse NP1 (without the signal sequence: Met1-Ala22), NP2 (without signal sequence: Met1-Ala14) and NPR (without the transmembrane domain, Met1-Ile23) were cloned into pCAGGS downstream of the Igκ secretion signal sequence, followed by a 2xHA tag.

Production of recombinant proteins

For large-scale production, proteins were expressed using established procedures for transient transfection (61) or lentiviral transduction (63) of HEK293 cells. Briefly, for large-scale transient transfections, the pHLsec expression plasmids encoding the proteins of interest ($NP1_{PTX}$, Nrx1β(+4), Nrx1β(–4), $GluA1_{ATD}$, $GluA2_{ATD}$, $GluA3_{ATD}$, $GluA4_{ATD}$, and $GluD2_{ATD}$) were transfected into 3-L adherent HEK293T (ATCC cat. # CRL-1573) expression cell cultures. The supernatants were collected 5 d post-transfection and filtered (0.22 μm). For the lentiviral infections, the pHR-CMV-TetO$_2$ transfer plasmid (Addgene cat. # 113887) encoding the protein of interest (CPTX), the psPAX2 packaging plasmid and the pMD2.G envelope plasmid were cotransfected into the HEK293T Lenti-X producer cell line (Takara Bio cat. # 632180). The supernatant containing the viral particles was harvested after 3 d, filtered (0.45 μm) and directly used for the infection of HEK293T expression cells. The infected cells were grown and expanded to 3-L adherent cell cultures. The supernatants were collected 5 d post-infection and filtered (0.22 μm). All supernatants were concentrated and buffer-exchanged using the AKTA flux system (GE Healthcare) or a QuixStand benchtop diafiltration system (GE Healthcare). Proteins were first purified by immobilized metal-affinity chromatography (IMAC) using pre-packed nickel Sepharose columns (GE Healthcare), or in batch mode on TALON beads (Takara Bio) collected on an EconoColumn (Bio-Rad). Then, elution fractions were pooled after SDS-PAGE analysis and concentrated, followed by further purification by size exclusion chromatography (SEC) using a Superdex 200 16/600 column (GE Healthcare) in 10 mM HEPES (4-(2-hydroxyethyl)-1-piperazineethanesulfonic acid) pH 7.4, 150 mM sodium chloride and 3 mM calcium chloride (HBS-C) for structural studies ($NP1_{PTX}$), or in 10 mM HEPES pH 7.4, 150 mM sodium chloride (HBS; vehicle) for biological studies (CPTX), or in 10 mM Tris pH 7.4, 150 mM sodium chloride, 3 mM calcium chloride and 0.005% (v/v) Tween-20 (TBS-CT) for interaction studies using SPR (Nrx1β(+4), Nrx1β(–4), $GluA1_{ATD}$, $GluA2_{ATD}$, $GluA3_{ATD}$, $GluA4_{ATD}$, and $GluD2_{ATD}$).

Protein crystallization

Crystallization trials, using 100 nL protein solution plus 100 nL reservoir solution in sitting drop vapor diffusion format, were set up in 96-well Greiner plates using a Cartesian Technologies robot (65). Purified human $NP1_{PTX}$ (Pro224-Ile431), produced from HEK293T cells and concentrated to 6.5 g/L, crystallised in 15% (v/v) glycerol, 25.5% (w/v) polyethylene glycol (PEG) 8000, 0.17M ammonium sulphate and 0.085 M sodium cacodylate pH 6.5. Crystals were cryoprotected using a reservoir solution containing 30% (v/v) ethylene glycol.

Crystallographic data collection and structure determination

Diffraction data for $NP1_{PTX}$ were collected at Diamond Light Source (DLS) beamline I03 to a nominal resolution of 1.45 Å in space group (SG) $C2$. All data were indexed, integrated, and scaled using the automated XIA2 expert system (66), using the Labelit (67), POINTLESS and AIMLESS (68, 69), and XDS (70) softwares. The structure of $NP1_{PTX}$ was solved by molecular replacement using Phaser (71) and using the human SAP (Serum Amyloid P Component; PDB code 1SAC) crystal structure (42) as a search model. Crystallographic data collection and refinement statistics are presented in Table S1.

Structure refinement and model analysis

Maximum-likelihood refinement of $NP1_{PTX}$ was initially performed with Refmac5 using "jelly body" restraints (72), and finally with phenix.refine (73) using automated X-ray and atomic displacement parameter (ADP) weight optimization applied throughout. Automated model building was performed using ARP/wARP (74) and further manual model building was performed using Coot (75). Structure validation was performed using the MolProbity routines within the PHENIX software suite (73, 76). Molecular representations were made using PyMOL (77).

Multi-angle light scattering (MALS)

Protein samples concentrated to ~1.0 g/L were injected into an HPLC-driven SEC column (Superdex 200 10/30 column, GE Healthcare) equilibrated with HBS-C buffer. The SEC column was coupled to an online UV detector (Shimadzu), an 18-angle light scattering detector (DAWN HELEOS; Wyatt Technology), and a refractive index detector (Optilab T-rEX; Wyatt Technology). CPTX contains an N-linked sugar on the Cbln1 N-terminal cysteine-rich region (CRR), and molecular mass determination was performed using an adapted RI increment value (*dn/dc* standard value; 0.185 mL/g) to account for the glycosylation state. $NP1_{PTX}$ and $NP1_{PTX-3Cl}$ are not glycosylated hence the standard *dn/dc* value was used for molecular mass determination. Data analysis was carried out using the ASTRA V software (Wyatt Technology).

Surface plasmon resonance (SPR)

cDNA for the immobilized proteins (CPTX, $NP1_{PTX}$, Cbln1) was cloned into the pHLsec-Avitag3 vector (61), resulting in proteins carrying a C-terminal biotin ligase (BirA) recognition sequence (Avitag). Constructs were co-transfected with pDisplay-BirA-ER (Addgene cat. # 20856; coding for an ER-resident biotin ligase) (78) for in vivo biotinylation in HEK293T cells in small-scale 6-well plates in a 3:1 pHLsec:pDisplay stoichiometric ratio. A concentration of 100 μM D-biotin was maintained in the expression medium to ensure biotinylation of the Avitag. After 48 h of expression, conditioned medium was collected and dialyzed against 10 mM Tris pH 7.4, 150 mM sodium chloride, 3 mM calcium chloride and 0.005% (v/v) Tween-20 (TBS-CT). SPR experiments were performed on a Biacore T200 (GE Healthcare) operated at a data collection frequency of 10 Hz. Streptavidin (Sigma-Aldrich cat. # S4762) was chemically coupled via amine coupling chemistry onto CM5 chips to a response unit (RU) level of 5000 RU. Then, biotinylated proteins were captured to the desired RU level. In each instance, for every two analyte binding cycles, a

buffer injection was performed, allowing for double referencing of the binding responses (79).

Antibodies

The origin, dilution, company and catalog number are as follows: Anti-calbindin (Goat, 1:500, Frontier Institute, Af1040), anti-HIS (Mouse, 1:1000, MBL, D291-3 or Rabbit, 1:1000, CST, 2365), anti-Myc (Rabbit, 1:1000, MBL, 562), anti-FLAG (Rabbit, 1:1000, Sigma-Aldrich, F7425), anti-HA (Mouse, 1:1000, BAbCo, MMS-101P), anti-synaptophysin (Mouse, 1:500, Sigma-Aldrich, S5768 or Guinea pig, 1:500, Frontier Institute, Af300), anti-neurexin (Chicken, 1:500, a gift from Dr. P. Scheiffele, University of Basel, Basel, Switzerland), anti-GFP (Rabbit 1:1000, Frontier Institute, Af-2020), anti-MAP2 (Goat, 1:500, Frontier Science, Af860), anti-PSD95 (Mouse, 1:500, Invitrogen, MA1-046), anti-pan-AMPAR (Guinea pig, 1:500, Frontier Institute, Af580), anti-GluA1 (Rabbit, 1:100, Calbiochem, PC246 or Guinea Pig, 1:500, Frontier Institute, Af380), anti-GluA2/3 (Rabbit, 1:1000, Chemicon, AB1506), anti-GluA4 (Rabbit, 1:1000, Pharmingen, 60666N or Guinea Pig, 1:500, Frontier Institute, Af640), anti-GluN1 (Mouse, 1:500, BD Biosciences, 556308 or Mouse, 1:500, Chemicon, MAB363), anti-VGluT1 (Rabbit, 1:500, Frontier Institute, Af570 or Goat, 1:500, Frontier Institute, Af310), anti-VGluT2 (Guinea Pig, 1:500, Frontier Institute, Af720 or Goat, 1:500, Frontier Institute, Af310), anti-VGAT (Goat, 1:500, Frontier Institute, Af620 or Guinea pig, 1:500, Frontier Institute, Af1000), anti-Parvalbumin (Goat, 1:500, Frontier Institute, Af460), anti-Homer 1 (Guinea pig, 1:1000, Synaptic Systems, 160-004) and anti-Bassoon (Rabbit, 1:500, Synaptic Systems, 141-003 or Mouse, 1:500, Enzo Life Sciences, SAP7F407). Anti-NP1 and NPR antibodies were newly raised by guinea pigs and rabbits immunized with peptides Glu185-Lys227 (NP1) or Ser226-Glu263 (NPR). For the simultaneous detection of various GluAs (GluA1–3 or GluA1–4), the mixture of the primary antibodies described above was used. Secondary antibodies conjugated with DyLight 405, Alexa 488, 546, 647 and Cy3 (Invitrogen or Jackson ImmunoResearch Laboratories) against the respective primary antibody were used in the dilution 1:1000 for immunocytochemistry or 1:200 for immunohistochemistry. Isospecific secondary antibodies against mouse IgG1 or IgG2a were used for the simultaneous staining of two types of mouse primary antibodies.

Immunoblotting

For fig. S15A-B, the hippocampus and conditioned medium were solubilized in laminae buffer (2% SDS, 80 mM Tris-HCl pH 6.8, 10% glycerol, 0.00625% Coomassie blue G 250) and the proteins were reduced by boiling for 3 min using 2% 2-mercaptoethanol. For fig. S22A, brain tissue from the hippocampus, cerebellum (vermis) and spinal cord were solubilized by 190–250 μL 1% SDS buffer, sonicated, and quantified for protein concentration. Samples were diluted in laminae buffer and reduced by boiling for 20 min using 2% 2-mercaptoethanol. Samples were subjected to gradient gel SDS-PAGE (Fujifilm Wako Chemicals) and blotted onto the membrane (Immobilon-P PVDF membranes, Merck Millipore). Membranes were blocked with TS-tween (0.1% Tween-20, 50 mM Tris-HCl pH7.6, 150 mM NaCl) containing 5% skimmed milk (CPMeiji) and subjected to the primary antibody for 2 h and HRP-conjugated secondary antibody (GE Healthcare) for 30 min. Chemiluminescence was generated by the ImmunoStar (Fujifilm Wako Chemicals) or

Immobilon (Merck Millipore) detection kits and detected by the LAS-3000 mini (Fujifilm) or iBright systems (Thermo Fisher Scientific).

Cell-based in vitro binding assays

HEK293 tsA201 cells (a gift from Dr. R. Horn, Thomas Jefferson University, Philadelphia, USA) were cultured in high glucose DMEM (Sigma-Aldrich) containing 10% FBS (HyClone), 50 U/mL Penicillin, 50 mg/mL Streptomycin (Invitrogen), 2 mM L-Glutamine in 10% CO_2 at 37°C. Cells were transfected with pDisplay encoding myc-tagged GluA1–4 ATD or with pCAGGS encoding GFP or FLAG-tagged Nrx, using Lipofectamin 2000 (Invitrogen). On the following day, transfected cells were detached by phosphate-buffered saline (PBS) containing 5 mM EDTA and seeded on 12-mm coverslips coated with poly-L-lysine (PLL; Sigma-Aldrich) at 2 x 10^4 cells/well. One hour after seeding, cells were treated with Mock (vehicle; HBS buffer), recombinant Cbln1-HIS or CPTX-HIS (23.6 nM, calculated for the hexamers) for 4 h to overnight. For the in vitro tripartite binding assay (fig. S3C), cells were further incubated with the conditioned medium containing Nrx1β(+4)-hFc for 4 h. Cells were fixed with 4% PFA/PBS for 15 min and washed with PBS three times. After blocking with 3% BSA/PBS (BSA: Sigma-Aldrich) for 30 min without permeabilization, cells were further incubated with primary antibodies against the ligand tag (HIS, HA and/or hFc) in 3% BSA/PBS for 2 h at room temperature (RT) or 24 h at 4 °C. Following three washes with PBS, cells were permeabilized with PBS containing 0.1% Triton-X 100 (Sigma-Aldrich) and 3% BSA. Cells were stained with primary antibodies against the receptor tag (FLAG or Myc) for 2 h at RT or 24 h at 4°C, followed by washing with PBS and incubation with the respective secondary antibodies for 30 min. Following washing with PBS, coverslips were mounted on a glass slide with Fluoromount-G. Samples in which HEK293 cells expressed GFP were not stained by primary antibodies against GFP but treated with the same primary antibodies against the receptor tag (FLAG or Myc) and the fluorescence of GFP was detected by microscopy.

In vitro synapse formation assays

Hippocampal culture—Preparation from embryonic day 16-17 (E16-17) wild-type ICR mice was performed as described (13) with some modifications. 2 x 10^5 neurons were plated on 12-mm cover glasses coated with PLL and maintained in Neurobasal cell culture medium (Invitrogen) containing NS21 supplement (80), 50 U/mL Penicillin, 50 mg/mL Streptomycin (Invitrogen), 2 mM L-Glutamine and 2% FBS (HyClone) in 5% CO_2 at 37°C. 1-2 h after the initial incubation, the culture medium was changed to fresh medium without FBS. For induction of presynapses by HEK293 cells (fig. S4), neurons were co-cultured with 2 x 10^4 HEK293 cells expressing GFP or Myc-tagged GluA1–4 or GluD2 ATDs at day-in-vitro (DIV) 4, 5 or 7 for 1 h, followed by treatment with vehicle or recombinant Cbln1-HIS or CPTX-HIS (23.6–30 nM, calculated for the hexamers), or with conditioned medium containing NP1-HA or CPTX-HIS secreted from HEK293 cells transfected with those plasmids for 2 d. For induction of AMPARs by HEK293 cells (fig. S6A), neurons were co-cultured with HEK293 cells expressing Nrx-3xFLAG and GFP, Cbln1-HIS or CPTX-HIS at DIV9 for 2 d. For synapse induction by beads, neurons were treated with streptavidin Dynabeads M-280 (Thermo Fisher Scientific) coated with Cbln1-HIS or CPTX-HIS through anti-HIS mAb-biotin (MBL) for 1–2 d (DIV20–22 for Syp, Nrx and GluA1–3 in Fig. 2B,

fig. S5A and fig. S6B, DIV4–6 for VGluT1 in fig. S5B, and DIV30–32 for GluA4 in fig. S6C). To label axons and dendrites, GFP was transfected with Lipofectamine 2000 at DIV6. Following the incubations, the cells were fixed with 4% PFA/PBS for 5 min at RT. Cells were washed with PBS and fixed with chilled methanol for 8 min on ice, followed by washing with PBS. Cells were permeabilized and blocked with PBS containing 0.1 % Triton-X 100, 3% BSA and stained with primary antibodies diluted in blocking buffer for 2 h at RT or 24 h at 4°C, followed by washing with PBS and incubation with secondary antibodies diluted in blocking buffer for 30 min. Following washing with PBS, coverslips were mounted on a glass slide with Fluoromount-G (SouthernBiotech).

Cerebellar culture—Cerebellar cultures were prepared from postnatal day 0–3 (P0–3) *Cbln1*-null mice (on the ICR genetic background) as described (13) with minor modifications. 2×10^5 neurons were plated on 12 mm cover glasses coated with PLL and were maintained in DMEM/F12 (Sigma-Aldrich) containing 100 μM putrescine, 30 nM sodium selenite, 0.5 g/mL triiodothyronine, 0.25 mg/mL BSA, 3.9 mM glutamate and N3 supplement (100 μg/mL apotransferrin, 10 μg/mL insulin and 20 nM progesterone) and 10% FBS in 5% CO_2 at 37°C. 1-2 h after incubation, the culture medium was changed to fresh medium without FBS. Co-culturing with HEK293 cells (at DIV 4 or 5 for 2 d), fixation, permeabilization and staining were performed as described above for the hippocampal culture.

Quantification of signal intensities of in vitro assays

Fluorescence images of cultured samples were captured using a CCD camera attached to a conventional fluorescence microscope (BX63, Olympus) or a confocal laser scanning microscope (FV1000, Olympus) using a 40× objective for the detection of HEK293 cells or using a 60× objective with 5× digital zoom for the detection of beads. The same parameters, such as exposure time and excitation power, were used for the sample set to be compared, except for GFP signals. Analyses were performed semi-automatically by a customized macro using Image J (Fiji). Background subtraction using the rolling ball method (radius = 20-100 pixels (px)) was applied to images to reduce the background noise. Regions of interest (ROIs) of beads or HEK293 cells expressing receptors were determined by the signal intensity and area size fulfilling the threshold (Otsu or Triangle) and particle definition. For quantification of signals on HEK293 cells, the signal intensity within the ROI was determined by subtracting the mean signal intensity outside the ROI. For quantification of signals on beads and to minimize non-specific signals associated with the cross-reactivity of beads with antibodies, the signal intensity was determined by subtracting the mean intensity of beads located in the field where no cells were present (Fig. 2B, fig. S5A-B and fig. S6B-C). For fig. S6C, ROIs of beads were manually classified into two groups, those contacting and non-contacting with PV$^+$ interneurons, which were identified by PV and GluA4 immunoreactivities. The signal intensity was calculated by subtracting the intensity on non-contacting beads from that on contacting beads.

Immunocytochemistry and immunohistochemistry

Hippocampal culture—Dissociated hippocampal neurons were prepared from E17 embryos, infected by AAV CAG-GFP at DIV12 to express GFP (Fig. 2C and fig. S7B) and

cultured for 21 DIV. They were incubated overnight (between DIV20 and 21) with 7 nM CPTX added directly to the culture medium. Neurons were either fixed with 4% PFA, permeabilized with 0.1% Triton-X 100 in PBS for 10 min, washed three times and blocked (0.1% Glycine + 0.1% Tween-20 + 10% normal goat serum in PBS for fig. S7A) for 45 min, or fixed with 4% PFA, fixed with chilled methanol, permeabilized and blocked (2% Goat serum 2% BSA + 0.1% Triton-X 100 in PBS for Fig. 2C and fig. S7B) for 30 min at RT. Cells were incubated 1 h or overnight with primary antibodies diluted in the blocking buffer and washed with PBS three times. Cells were incubated with respective secondary antibodies for 1 h at RT. Coverslips were washed with PBS, incubated with or without DAPI (Invitrogen, cat. # D1306) for 10 min and mounted using Fluoromount aqueous mounting media (Sigma Aldrich, cat. # F4680) or Fluoromount-G (SouthernBiotech). For the acquisition of the images in fig. S7A, a complete Z stack spanning primary hippocampal cultures was acquired on a Leica TCS SP8 3X microscope equipped with a 405 nm diode laser and a white light laser (WLL) for excitation. The format for all images was set to 1024 x 1024 pixels with an optical zoom of 2× resulting in a pixel size of 90 nm in the x-y plane. Images were taken at 400 lines/s and line averaging of 2. To improve image quality for representation, raw confocal images were deconvoluted using the Huygens Professional software (SVI, v15.10). The theoretical point spread function (PSF) parameters were automatically acquired from confocal LIF-files. Within the deconvolution wizard, images were subjected to manual background correction and signal-to-noise ratio optimization. The "optimized iteration" mode of the Good's roughness Maximum Likelihood Estimation algorithm (GMLE) was applied until it reached a quality threshold of 0.01. For the representation of the images, the contrast was enhanced for the complete image by linear methods using Fiji for each channel separately. For the acquisition of the images in Fig. 2C and fig. S7B, a confocal laser scanning microscope (FV1000, Olympus) was used to acquire single-plane images around GFP-positive dendrites without the cell body, using a 100× objectives with 4× optical zoom.

Hippocampal sections—For fig. S10A, Thy1-GFP mice were transcardially perfused 3 d after CPTX injection with 4% PFA in 0.1 M sodium phosphate buffer (PB; pH 7.2) for 10 min under deep isoflurane anesthesia. The dissected brains were incubated in PBS containing 4% PFA, cryoprotected in PBS containing 30% sucrose for 48 h, frozen at –80°C and cut into 50 μm thick sections by cryostat (Leica). Membrane permeabilization was performed with 0.5% Triton-X 100 in PBS for 30 min. Sections were blocked with blocking buffer (0.1% Glycine + 0.1% Tween-20 + 10% normal goat serum in PBS) for 90 min. Above mentioned antibodies were used for the detection of Bassoon (1:500) and HIS (1:500), diluted in blocking buffer and applied for 2 d at 4°C. Sections were washed three times with PBS followed by incubation with the respective secondary antibodies (1:1000) for 3 h at RT. Sections were mounted using Fluoromount aqueous mounting media (Sigma Aldrich, cat. # F4680). Complete Z stacks spanning 50 μm thin hippocampal slices were acquired on a Leica TCS SP8 3X microscope. For acquiring images, the Leica objective HC PL APO CS2 63×/1.40 oil was used. Bassoon (405 nm), Thy1-GFP (488 nm), CPTX (546 nm) images were acquired using the confocal scanning mode. The format for all images was set to 512×512 pixels with an optical zoom of 3.04 resulting in a pixel size of 119 nm in the x-y plane. Images were taken at 400 lines/s and line averaging of 4.

For fig. S10B, fig. S11, fig. S12 and fig. S17 1 d after the unilateral hippocampal injection of CPTX into WT mice, and for fig. S18, 3 d after the unilateral hippocampal injection of CPTX into 5xFAD mice (11–12 months old), the brain was freshly frozen with liquid nitrogen after decapitation under deep isoflurane anesthesia. Sections (10–20 μm thick) were cut by cryostat (Leica), mounted on glass slides or coverslips and postfixed with 4% PFA in sodium phosphate buffer (PB; pH 7.2) or 3% glyoxal for 15 min to 2 h at RT. Following washing with PBS + 0.1% Triton X-100, sections were treated with 10% donkey serum for 30 min at RT, incubated with a mixture of primary antibodies overnight and with a mixture of respective secondary antibodies for 2 h. Finally, the sections were attached to the glass slides and mounted with Fluoromount-G, VECTASHIELD (Vector Laboratories) or ProLong glass (Invitrogen). Fluorescence images were captured using confocal microscopy (SD-OSR, Olympus or LSM880, ZEISS) using the same parameters such as objectives, zoom, laser power, exposure time, gain and offset for the comparison of samples. Super-resolution images were obtained by structural illumination with SDOSR (Objective: $100\times/$ 1.49 oil with $3\times$ zoom lens, pixel size: 40 nm/px, configuration: XY < 120 nm, Z < 300 nm) or by Airyscan with LSM880 ($63\times/1.40$ oil with $3\times$ digital zoom, 35 nm/px, XY < 120 nm, Z < 350 nm). Images obtained by Airyscan were 3D-reconstructed by Imaris (Bitplane).

For the quantification of pre- and postsynaptic molecule clustering (fig. S12, fig. S17 and fig. S18), images were obtained using a $100\times$ objective around the area of the injected side of the hippocampus (*Str. radiatum* or *Str.lacunosum moleculare*) and the corresponding area of the contralateral uninjected or control-injected side. Injected areas were confirmed by the HIS immunoreactivity. The dynamic range of signals was first determined by maximal and minimal signal intensities in pair images of the injected and the contralateral area and then each signal intensity was normalized to this value (max-min). Normalized intensity histograms were calculated by dividing the normalized signal intensity into 40 bins on a logarithmic scale. Thus, the signal intensity in the nth bin equals $10^{(n \times (max-min) / 40)}$. To analyze the bright pixels, the mean intensity + 3 SD of the contralateral area was used as the threshold. Selected pixels were analyzed as particles using the "Analyze Particles" command within Image J without any constraint on size or circularity, leading to the calculation of particle size, number, area fraction and intensity.

Cerebellar sections—One day after the cerebellar injection of vehicle or CPTX into *Cbln1*-null mice or *GluD2*-null mice (3- or 7-month old), they were transcardially perfused with 4% PFA in 0.1 M sodium phosphate buffer (PB; pH 7.2) for 10 min under deep pentobarbital anesthesia, followed by post-fixation of dissected brain samples with 4% PFA in PB for 2 h at 4°C. Alternatively, the brain was freshly frozen with liquid nitrogen after decapitation under deep isoflurane anesthesia. Free-floating sections (50 μm thickness) from 4% PFA fixed brains were prepared with a microslicer (DTK-1000, Dosaka EM), followed by treatment with 1 mg/mL pepsin (Dako) in PBS containing 0.1% Triton X-100 and 0.2 N HCl for 10 min at 37°C, washing of the sections with PBS containing 0.1% Triton X-100 and blocking with 10% donkey serum for 30 min at RT. Sections of freshly frozen brains were prepared by cryostat (Leica) at 20 μm thickness, mounted on glass slides and fixed with 3% glyoxal for 15 min, followed by blocking with 10% donkey serum for 30 min at RT and permeabilization with PBS containing 0.1% Triton X-100 (wash buffer). Sections were

incubated with a mixture of primary antibodies diluted in wash buffer overnight, washed three times, incubated with a mixture of respective secondary antibodies in wash buffer and again washed three times. Finally, the sections were mounted with VECTASHIELD (Vector Laboratories). Fluorescence images were captured using a confocal laser scanning microscope (FV1000, Olympus) using the same parameters such as objectives, zoom, laser power, gain and offset for the comparison of samples. Colocalization of signals was analyzed by the plugin "Coloc 2" in Image J (81).

Cortical sections—One-month-old mice, into which miR vectors were transfected by in utero electroporation, were transcardially perfused with 3% glyoxal for 10 min under deep pentobarbital anesthesia, followed by post-fixation of the dissected brain with 3% glyoxal for 2 h at 4°C. Free-floating sections (100 μm thickness) were prepared with a microslicer (DTK-1000, Dosaka EM). Following washing of the sections with PBS containing 0.1% Triton X-100 (wash buffer), sections were subsequently treated with 10% donkey serum for 30 min at RT, incubated with a mixture of primary antibodies diluted in wash buffer overnight, washed three times, incubated with a mixture of respective secondary antibodies in wash buffer and again washed three times. Finally, the sections were attached to glass slides and mounted with VECTASHIELD (Vector Laboratories). Z-stacked fluorescence images of NP1 and NPR were obtained throughout the brain slice in the transfected cortical area at every 2 μm using a confocal microscope (SD-OSR, Olympus) using 20× objectives. Soma area regions of interest (ROIs) in layers 2/3 with abundant expression of NP1/NPR were found in a large population of neurons and were manually selected in an unbiased manner according to the GFP signal. Signal intensities of NP1/NPR were quantified using Image J. Background signals were subtracted using the rolling ball method (radius = 50 px) and the signals were normalized to the surrounding signals enlarged to 5 px because the absolute signal intensity was strongly affected by the z-position of the ROI in the brain section at 100 μm thickness.

Spinal cord sections—2–5 d after the injection the mice were transcardially perfused with 3% glyoxal for 10 min under deep pentobarbital anesthesia, followed by post-fixation of the dissected spinal cord with 3% glyoxal overnight at 4°C and by cryoprotection in 30% sucrose/PBS for several days. Spinal cords embedded in Tissue-Tek O.C.T. compound (Sakura Finetek, cat. # 4583) were horizontally or coronally sectioned by cryostat (Leica) at 20–40 μm thickness in 4–5 mm around the epicenter of the injury and the slices were mounted on APS-coated glass slides (Matsunami) at 200–400 μm intervals. Following washing with PBS + 0.1% Triton X-100, sections were treated with 10% donkey serum for 30 min at RT and incubated with a mixture of primary and respective secondary antibodies overnight. Finally, the sections were attached to glass slides and mounted with Fluoromount-G (SouthernBiotech). Fluorescence images of all sections were captured and digitized as a virtual slide (OlyVIA, Olympus) using a conventional fluorescence microscope (BX63, Olympus) with a 4× objective to determine the section at 1.4–1.6 mm upstream of the precise epicenter of the injury. Fluorescence images of the section were subsequently captured using a confocal microscope (SD-OSR, Olympus; 63× objective) around the gray matter ventral root using the same parameters such as objectives, laser power, exposure time, gain and offset for the comparison of samples. The super-resolution images were obtained

by Airyscan 2 with a confocal laser scanning microscope (LSM980, ZEISS; 63×/1.40 oil objective with 2.5x digital zoom, 35 nm/px, XY < 120 nm, Z < 350 nm). To define the particles of GluA4, VGluT2 and their intersections, the fluorescent images were subjected to background subtraction (50 px), Laplace filtering (9 x 9), box filtering (5 x 5), auto thresholding (Otsu method), particle extraction (> 5 px), binarization and segmentation by watershed. The defined particles were used as ROI to quantify the size and mean intensity of each channel. The percentage of GluA4+/VGluT2+-double-positive puncta was calculated as the number of VGluT2 particles accompanied by more than 1 px of defined GluA4 particles in the ROI, divided by the total number VGluT2 particles. All image processing was performed by ImageJ. For fig. S16D, E, slices of the spinal cord and hippocampus from the same mouse were mounted on glass slides, stained using the same procedures and the images were taken using the same microscope settings.

Golgi-Cox staining and dendritic spine analysis

WT and 5xFAD mice (11–12 months old) were sacrificed and decapitated 3d after CPTX or Mock injection. Brains were quickly removed from the skull and washed with bi-distilled water to remove blood from the surface. Golgi-Cox impregnation of neurons was performed using the FD Rapid GolgiStain kit (FD NeuroTechnologies, cat. # PK401). Dye-impregnated brains were rapidly frozen on methyl butane and dry ice, embedded in Tissue-Tek O.C.T. compound (Sakura Finetek, cat. # 4583), cryo-sectioned coronally at 100 μm thickness and directly mounted on gelatin-coated slides (FD NeuroTechnologies, cat. # PO101) with the help of solution C provided in the kit. Sections were stained according to the manufacturer's protocol and mounted using the ROTI Histokitt embedding medium (Carl Roth, cat. # 6638). Secondary apical dendrites from CA1 pyramidal neurons with cell bodies located in the dorsal part of the hippocampus were imaged for spine analysis. Sections were imaged by an experimenter blinded to experimental conditions using a Leitz DMRXE microscope (Leica) as Z stacks with 0.25 μm intervals and at a magnification of 100×. 7-8 dendrites of 60–80 μm length were imaged for each animal. The analysis was done by an experimenter blinded to experimental conditions using the Neurolucida software v11 (MBF Bioscience). Dendritic spines were defined as the protrusions greater than 0.4 μm that emerged from the dendrites and were identified going through the focal planes of the Z stacks. To facilitate visual inspection of the Z-minimal projections in Fig. 4A and of the 3D images in Movie S4, the background was removed using the rolling ball method (radius = 30 px) and images were corrected using an unsharp mask filter (radius = 2 px, mask weight = 0.7) in Fiji (81). Then, 3D projections (made using the 3D projection tool in Fiji) were additionally processed using the rolling ball method (radius = 15 px), an unsharp mask filter (radius = 1 px, mask weight = 0.6) and contrasted to remove a remaining blur around dendritic shafts and enhance the visibility of small protrusions.

Electron microscopy

For the in vivo Cbln1 and CPTX administration experiments, *Cbln1*-null or *GluD2*-null mice (C57BL/6J genetic background, 3-6 months old) were perfused transcardially with 2% PFA + 2% glutaraldehyde in 0.1 M PB (pH 7.2) under deep pentobarbital anesthesia 3 d after the injection into the cerebellum. Parasagittal microslicer sections of the cerebellum (300 μm thickness) were postfixed for 2 h with 1% OsO_4 in 0.1 M PB. After block staining in 1%

aqueous uranyl acetate solution and dehydration with graded alcohols, the sections were embedded in Epon 812. Serial ultrathin sections (70 nm) were made using an ultramicrotome and stained with 2% uranyl acetate for 5 min and mixed lead solution for 2 min. Electron micrographs of the molecular layer were taken using an H-7100 electron microscope (Hitachi) at a magnification of 4,000× and printed at a magnification of 16,000×. For the quantitative analysis of PF–Purkinje cell synapses, the asymmetrical postsynaptic density in the cerebellar cortex was randomly photographed and the frequency of contacted and naked/free synapses was analyzed using the MetaMorph software as described previously (16). Three series of serial sections, each of which consisted of ten electron micrographs, were analyzed (n = 1–2 mice).

Ex vivo electrophysiology

Hippocampus (Figs. 4 and S13-14)—All experiments were performed in 4- to 6-week-old C57BL/6J WT mice, 4- to 6-week-old PV-*Cre*/tdTomato-FLEX double transgenic mice (for miniature excitatory postsynaptic current (mEPSC) recordings from CA1 PV+ interneurons), 5-month-old 5xFAD mice (for mEPSC recordings), or 15- to 18-month-old 5xFAD transgenic mice (for long-term potentiation (LTP) recordings), as described previously (82). Animals were sacrificed and then decapitated. Hippocampi from both hemispheres were isolated and placed on an agar block to cut transverse slices (350 μm thick) using a vibrating microtome (VT1200S, Leica) in an ice-cold solution containing 2 mM KCl, 1 mM $MgCl_2$, 2 mM $MgSO_4$, 1.25 mM NaH_2PO_4, 26 mM $NaHCO_3$, 1 mM $CaCl_2$, 10 mM D-glucose, and 230 mM sucrose for mice younger than 6 months or 2.5 mM KCl, 10 mM MgSO4, 1.2 mM NaH_2PO_4, 30 mM $NaHCO_3$, 0.5 mM $CaCl_2$, 20 mM HEPES, 25 mM glucose, 93 mM NMDG, 5 mM sodium ascorbate, and 3 mM sodium pyruvate for 15- to 18-month-old mice (pH 7.4 with HCl). All solutions were saturated with 95% O_2 and 5% CO_2 and the osmolality was adjusted to 300 ± 5 mOsm. For in vitro CPTX treatments, slices were incubated in a 2-mL chamber for 4 h at room temperature in the artificial cerebrospinal fluid (ACSF) solution containing 124 mM NaCl, 2.5 mM KCl, 1.3 mM $MgSO_4$, 1 mM NaH_2PO_4, 26.2 mM $NaHCO_3$, 2.5 mM $CaCl_2$, and 11 mM D-glucose. CPTX was added at 20 μg/mL to slices in the chamber, whereas control slices were incubated in ACSF without CPTX. Next, the slices were transferred to the recording chamber and were continuously perfused with the same ACSF for mEPSC measurements. Picrotoxin (50 μM, Tocris Bioscience), CGP 55845 (3 μM, Tocris), and tetrodotoxin (Tocris) were added to ACSF to block $GABA_A$, $GABA_B$ receptor and Na^+ channels, respectively, and hence to isolate mEPSCs. Whole-cell patch recordings from CA1 pyramidal neurons were obtained using glass electrodes (4–6 MΩ, outer diameter of 1.5 mm, wall thickness of 0.315 mm; Hilgenberg). The glass electrodes were filled with a solution containing 140 mM K-gluconate, 8 mM NaCl, 0.2 mM $CaCl_2$, 10 mM HEPES, 5 mM lidocaine *N*-ethyl bromide (QX-314 Br), 0.5 mM Na_2GTP, and 2 mM Mg_2ATP (pH 7.2, 290 mOsm). The membrane potential was clamped at –70 mV. For miniature inhibitory postsynaptic current (mIPSC) recordings, NBQX (25 μM, AMPAR antagonist, Tocris), D-AP5 (50 μM, NMDAR antagonist, Tocris) and CGP 55845 were added to the ACSF solution. The glass electrodes were filled with a solution containing 120 mM CsCl, 8 mM NaCl, 0.2 mM $MgCl_2$, 10 mM HEPES, 2 mM EGTA, 5 mM QX-314 Br, 0.3 mM Na_2GTP, and 2 mM Mg_2ATP (pH 7.2,

290 ± 3 mOsm). mEPSC and mIPSC events were analyzed offline using the Mini Analysis software (v6.0.3, Synaptosoft).

ACSF solution containing 120 mM NaCl, 2.5 mM KCl, 1.5 mM $MgCl_2$, 1.25 mM NaH_2PO_4, 24 mM $NaHCO_3$, 2 mM $CaCl_2$, and 25 mM D-glucose was used for field excitatory postsynaptic potential (fEPSP) recording. Thin glass electrodes (outer diameter 1.5 mm, wall thickness 0.188 mm, ~2 MΩ) filled with ACSF were used for stimulation and recording of fEPSPs. The Shaffer collaterals pathway was stimulated using a glass electrode and theta-burst stimulation (TBS) trains were applied three times to induce LTP (83). The stimulation intensity was determined based on the input-output curve and was set to give fEPSPs with a slope of ~50 % of the supramaximal fEPSP. Single stimuli were repeated every 20 s for at least 10 min for baseline recording before and for 60 min after LTP induction. The paired-pulse ratio (PPR) was evaluated at 50-ms intervals under the same conditions. All recordings were obtained at $30 \pm 1°$C using an EPC-10 amplifier (HEKA Elektronik). The recordings were filtered at 1–3 kHz and digitized at 10-20 kHz.

Cerebellum—Parasagittal cerebellar slices (200 μm thick) were prepared from 4- to 6-weekold *GluD2*-null or *Cbln1*-null mice at 3 d after vehicle, Cbln1, NP1$_{PTX-3Cl}$ or CPTX injection, as described previously (84). Whole-cell patch-clamp recordings were made from PCs using a 60× water-immersion objective attached to an upright microscope (BX51WI, Olympus) at RT. The resistance of the patch pipettes was 1.5–3 MΩ when filled with an intracellular solution composed of 150 mM Cs-gluconate, 10 mM HEPES, 4 mM $MgCl_2$, 4 mM Na_2ATP, 1 mM Na_2GTP, 0.4 mM EGTA, and 5 mM QX-314 Br (pH 7.3, 298 mOsm/kg) for measurements of the input-output relationship and paired-pulse ratio of PF-EPSC amplitudes, and of 65 mM Cs-methanesulfonate, 65 mM K-gluconate, 20 mM HEPES, 10 mM KCl, 1 mM $MgCl_2$, 4 mM Na_2ATP, 1 mM Na_2GTP, 5 mM sucrose, and 0.4 mM EGTA (pH 7.25, 295 mOsm/kg) for long-term depression (LTD) recordings. The solution used for the slice storage and recording consisted of 125 mM NaCl, 2.5 mM KCl, 2 mM $CaCl_2$, 1 mM $MgCl_2$, 1.25 mM NaH_2PO_4, 26 mM $NaHCO_3$ and 10 mM D-glucose, bubbled continuously with a mixture of 95% O_2 and 5% CO_2. Picrotoxin (100 μM, Sigma Aldrich) was always present in the saline to block the inhibitory inputs. To evoke the PF-EPSCs, square pulses were applied at various stimulus intensities (10 μs, 0–200 μA) through a stimulating electrode placed on the molecular layer (~50 μm away from the pial surface). Selective stimulation of the PFs was confirmed by paired-pulse facilitation (PPF) of EPSC amplitudes at a 50-ms inter-stimulus interval. Current responses were recorded with an Axopatch 200B amplifier (Molecular Devices), and pClamp software (v9.2, Molecular Devices) was used for data acquisition and analysis. Signals were filtered at 1 kHz and digitized at 4 kHz.

CPTX injection

Acute intrahippocampal injection—We used a digitally controlled infusion system (UltraMicroPump III with Micro4 Controller, World Precision Instruments) fed with a 10 μL Hamilton syringe and a NanoFil (35 gauge) beveled needle. The mice were first anesthetized with 1–3 % isoflurane and placed into the stereotaxic frame (Narishige). 1 μL CPTX (1.49 mg/mL) or vehicle (HBS buffer) was bilaterally injected at a rate of 3 nL/s. We used the

following coordinates for bilateral injection: AP = –2.0 mm from Bregma and L = ±1.5 mm; DV = 2.0 mm from the brain surface according to the mouse brain atlas (85).

Acute intracerebellar injection—Mice were anesthetized with an intraperitoneal injection of ketamine/xylazine (80/20 mg/kg body weight, Daiichi-Sankyo or Sigma Aldrich). A small hole in the occipital bone was made with a dental drill, and the dura matter was ablated as described previously (16). A glass needle was inserted into the vermis of lobule VI/VII at ± 0.7 mm from the midline at a depth of ~200 μm. Approximately 7 μL of vehicle, Cbln1-HIS or CPTX-HIS (7.7 μM) was bilaterally injected at a rate of 10–40 μL/h.

Acute intrahippocampal injection through guide cannulas—Intrahippocampal guide cannulas were implanted as described previously (86–88) with minor changes. In brief, mice were anesthetized with 1–3% isoflurane mixed with O_2 through a vaporizer (Matrx VIP 3000, Midmark). Prior to any surgical manipulation, the mice were given the analgesic carprofen (5 mg/kg body weight (b.w.), subcutaneous injection (s.c.), Rimadyl, Pfizer Pharma) and the skin was cleaned by 75% ethanol, followed by 10% povidone iodine (Dynarex) and additional analgesic lidocaine (Xylocaine spray, 10 mg/metered dose, AstraZeneca). The mice were placed in a stereotaxic frame (Narishige), and all procedures were performed under a surgical binocular microscope (Labomed Prima DNT, Labo America) and on a heating pad (DC Temperature Controller, World Precision Instruments) to maintain mouse body temperature at 34–36 °C. The mouse scalp skin was circularly incised (φ 10 mm) and removed. The edges of the skin were processed with 75% ethanol and xylocaine. The scalp bone was carefully cleaned with 75% ethanol and 3% H_2O_2 and dried under 40°C (HG 2310 LCD, Steinel). After marking coordinates for implantation, 4 small holes for anchoring screws were drilled in the frontal and parietal bones by using a dental micro motor (Eickemeyer). Then all four screws were covered with acrylic dental cement Paladur (Heraeus Kulzer) leaving the marked areas for cannulas free of acrylic. Implantation began with drilling of a hole for the left cannula. The cannula was stereotaxically implanted by using a self-made universal holder for cannulas (small curved tweezers with a metal ring from Fine Science Tools). During implantation, the cannula gently touched the surface of the brain and only then it was secured with a small amount of acrylic. Next, the right cannula was similarly implanted and secured with acrylic. Coordinates for bilateral cannulas (AP: 2.0 mm; L: ±1.5 mm from bregma, the bottom end of cannulas should touch the surface of the brain), were set according to the mouse brain atlas (85). After implantation of cannulas, more dental cement was added to secure the whole system on the bone. After the surgery which took ~60 min, mice were returned to their home cages. Carprofen (5 mg/kg b.w. s.c., Rimadyl, Pfizer Pharma) was used as a postoperative analgesic. The intrahippocampal injections and behavioral tests were performed after the mice had fully recovered at least 5–7 d after surgery. Injections were done using a 10 μL Hamilton syringe as described in the *Acute intrahippocampal injection* section but being inserted in the guide cannula under brief sedation with 1% isoflurane.

Acute intraspinal injection to SCI mice—0.5 μL of CPTX (1 μg/μL), Cbln1 (1 μg/μL), Chondroitinase ABC (0.5 U/μL; Sigma Aldrich cat. # C2905) or vehicle (HBS buffer) were injected in the proximity of the injury site by electrical micro-injector (BJ-110, BEX Co.)

through glass capillaries (Drummond Scientific Company, cat. # 3-000-203-G/X). Following injection, the muscle layers and skin were again closed by suturing.

In utero electroporation

In utero electroporation (IUE) was performed at E14.0 in the cortex of ICR mice as described previously (89). Briefly, plasmid DNA was injected into the third ventricle by a glass pipette and a set of electrical pulses was applied 5 times. Positive electrodes were placed onto the cortical side. Plasmid DNA was dissolved in 21 mM HEPES, 137 mM NaCl, 5 mM KCl and 0.7 mM Na_2HPO_4 at a concentration of 1 mg/mL.

Surgical procedure for spinal cord injury (SCI)

Mice (9–11 weeks old) were subjected to hemisection- or compression-induced SCI. After the anesthesia, the spinal cord was surgically exposed and the dorsal column at the 10th thoracic vertebra (T10) was dissected by micro-scissors and a scalpel. The muscle layers and skin were closed by sutures. Animals were recovered from the anesthetic by the administration of the antagonist. Mice were subjected to compression-induced damage using an SCI impactor device (Infinite Horizon Impactor; Precision Systems and Instrumentation) (90) and using a 70-kdyn impact force. We monitored the strength and the duration of the impact of compression through the automated recording system in the SCI impactor device.

Behavioral Analysis

Spatial navigation in a labyrinth—The 3D-printed dry maze was developed at the DZNE. In short, before implantation of cannulas, mice were put on the light food restriction diet (LFRD) scheme where *ad libitum* food was removed from mice and was given daily manually at the same time in amounts comparable with normal consumption (4–5 g/day/ mouse). The weight of all mice was monitored daily and kept within a 10–15% reduction. Before the cannulation of mice, labyrinth habituation and training was performed for 2-3 weeks. Once all mice got familiar with the labyrinth, the room was changed to introduce new landmarks and cues, and the configuration of the labyrinth was changed to be more complex (Fig. 5A). Testing in the labyrinth began on d 3 after CPTX or Mock injection. Mice were placed into a starting zone in the labyrinth and given 20 min to find a hidden colorless and odorless round pellet reward (AIN-76A 10 mg tablet, TestDiet, cat. # 1811213). 2 h later the mice were placed again in the same labyrinth with the same room landmarks and cues for 10 min to find the reward. On d 4, the mice were placed again into the same labyrinth in which the reward zone was changed, and the mice had to re-learn the new position of the reward within 10 min. 2 h later, during the retrieval session (5 min), the mouse had to find the new location of the reward.

The position of mice in the labyrinth was recorded using a USB video camera (Microsoft) and special behavioral video acquisition and analysis software (ANY-maze). All recorded movies were analyzed using ANY-maze by a trained observer blind to the mouse genotype and treatments. ANY-maze was run in tracking mode to trace coordinates of mice (10 frames/s) and compute distance traveled from the starting zone to the hidden reward zone. The criteria for successful performance were that during encoding and retrieval sessions, the hidden rewards (7–8 pellets) were found and eaten. Travel distances in meters were

computed as follows: mice had to find the reward and take at least 1 pellet. This time point, as a beginning of the association of the reward location in the labyrinth and all landmarks and cues in the room, was used to calculate travel distances.

Contextual fear conditioning—To validate the action of CPTX in another hippocampusdependent cognitive task, we chose contextual fear conditioning (CFC). Shortly after spatial navigation in the labyrinth, at day 5 all mice were first recorded in a neutral context (context B, 5 min) and then 1 h later they were put into a conditioned context (context A, 5 min) and given three foot shocks, each with 0.5 mA and 1 s in duration and separated by 1 min. Contexts A and B were different in terms of walls (chess-like black-and-white pattern versus grey color), smell (different cleaning solutions) and floor (context A; metal grid to deliver foot shock, context B: white plastic floor. At day 6, 1 day after CFC, mice were first put in the context A for 5 min, then at least 1 h later in the context B for 5 min for retrieval sessions. CFC memory in retrieval sessions was measured as the fraction of the time a mouse was freezing in contexts A and B. Freezing of mice was defined as total immobility of animals (except for breathing) with a characteristic tense fearful posture. The analysis of data was done by using ANY-maze software. The fear conditioning system consisted of a touch-pad controller and a conditional sound-attenuated cabinet and chambers (Ugo Basile).

Rotor-rod test and gait analyses—To examine the skilled motor coordination in the mice, the rotor-rod test was performed. As this phenotype is clearly observed on the ICR genetic background (13, 16, 84), we used in 4- to 6-week-old *Cbln1*-null mice with this background. The rotor-rod test was performed 1 d before and 3 d after the injection. Six trials were performed at 20 rpm with a 30-s interval between trials, and the latency to fall from the rotor-rod was measured (maximum score; 120 s). For gait analyses, we used 4- to 6-month-old *Cbln1*-null and *GluD2*-null (C57BL/6J) mice. In addition, 4- to 6-week-old *Cbln1*-null mice (ICR) were used. Mice were habituated to the experimenter and the behavior room from 2–3 d before the test. Then, the mice were habituated to the gait analysis apparatus made of transparent plexiglass (6 cm x 85 cm) and trained to walk straight to their home cage. Each step during the walking was recorded by a video camera across the transparent floor at 30 frames per second. The time points and locations of the hind limb to attach and detach on the floor were manually determined by an experimenter blinded to experimental conditions, using custom software written in HSP (Hot Soup Processor, ONION software). These analyses were performed > 4 times for each mouse 1 d before and 3 d after Mock, Cbln1 or CPTX injection. Gait parameters were calculated as follows: (i) the coordinated step ratio was calculated as the number of alternate left/right steps divided by the number of total steps; (ii) the stride length of each step along the x-axis (plus direction to home cage); (iii) the stride speed and (iv) stride irregularity (the standard deviation of stride length during the single journey divided by the average stride length).

Locomotor recovery after SCI—The locomotor recovery assessment was performed using video recording as previously reported (90). BMS (Basso Mouse Scale) open-field scoring and footfall tests were performed weekly during the 6–8 weeks following SCI. The BMS score was evaluated by at least two independent investigators who were blinded to the

experimental groups. Mice were excluded if they had an incomplete injury (BMS score > 0) on day 2 after SCI. To quantify the recovery effect, the increase in BMS score between the 1st and 2nd week after SCI was calculated as: BMS/week = BMS score (2nd week) – BMS score (1st week).

For footfall tests, mice were placed on a wire-mesh grid and videotaped for 5 min while on the grid. Mice that walked longer than 3 min with more than 70 steps were subjected to scoring by three independent examiners. The total number of footfalls from the bars during the total walking time was counted.

Supplementary Material

Refer to Web version on PubMed Central for supplementary material.

Acknowledgments

Data and materials availability

All data are available in the main text or the supplementary materials. All the plasmids and antibodies generated in this study are available from the authors upon request. Structure factors and coordinates of $NP1_{PTX}$ are deposited in the Protein Data Bank (PDB code 6YPE).

References and Notes

1. Nelson SB, Valakh V. Excitatory/inhibitory balance and circuit homeostasis in autism spectrum disorders. Neuron. 2015; 87:684–698. [PubMed: 26291155]

2. Palop JJ, Mucke L. Network abnormalities and interneuron dysfunction in Alzheimer disease. Nat Rev Neurosci. 2016; 17:777–792. [PubMed: 27829687]

3. Bozzi Y, Provenzano G, Casarosa S. Neurobiological bases of autism-epilepsy comorbidity: a focus on excitation/inhibition imbalance. Eur J Neurosci. 2018; 47:534–548. [PubMed: 28452083]

4. Foss-Feig JH, et al. Searching for cross-diagnostic convergence: neural mechanisms governing excitation and inhibition balance in schizophrenia and autism spectrum disorders. Biol Psychiatry. 2017; 81:848–861. [PubMed: 28434615]

5. Forrest MP, Parnell E, Penzes P. Dendritic structural plasticity and neuropsychiatric disease. Nat Rev Neurosci. 2018; 19:215–234. [PubMed: 29545546]

6. Sudhof TC. Towards an understanding of synapse formation. Neuron. 2018; 100:276–293. [PubMed: 30359597]

7. Yuzaki M. Two classes of secreted synaptic organizers in the central nervous system. Annu Rev Physiol. 2018; 80:243–262. [PubMed: 29166241]

8. Jang S, Lee H, Kim E. Synaptic adhesion molecules and excitatory synaptic transmission. Curr Opin Neurobiol. 2017; 45:45–50. [PubMed: 28390263]

9. Sudhof TC. Synaptic neurexin complexes: a molecular code for the logic of neural circuits. Cell. 2017; 171:745–769. [PubMed: 29100073]

10. Takahashi H, Craig AM. Protein tyrosine phosphatases PTPdelta, PTPsigma, and LAR: presynaptic hubs for synapse organization. Trends Neurosci. 2013; 36:522–534. [PubMed: 23835198]

11. Johnson-Venkatesh EM, Umemori H. Secreted factors as synaptic organizers. Eur J Neurosci. 2010; 32:181–190. [PubMed: 20646052]

12. Siddiqui TJ, Craig AM. Synaptic organizing complexes. Curr Opin Neurobiol. 2011; 21:132–143. [PubMed: 20832286]

13. Matsuda K, et al. Cbln1 is a ligand for an orphan glutamate receptor delta2, a bidirectional synapse organizer. Science. 2010; 328:363–368. [PubMed: 20395510]

14. Uemura T, et al. Trans-synaptic interaction of GluRdelta2 and Neurexin through Cbln1 mediates synapse formation in the cerebellum. Cell. 2010; 141:1068–1079. [PubMed: 20537373]

15. Elegheert J, et al. Structural basis for integration of GluD receptors within synaptic organizer complexes. Science. 2016; 353:295–299. [PubMed: 27418511]

16. Ito-Ishida A, et al. Cbln1 regulates rapid formation and maintenance of excitatory synapses in mature cerebellar Purkinje cells *in vitro* and *in vivo*. The Journal of neuroscience: the official journal of the Society for Neuroscience. 2008; 28:5920–5930. [PubMed: 18524896]

17. Miura E, Iijima T, Yuzaki M, Watanabe M. Distinct expression of Cbln family mRNAs in developing and adult mouse brains. Eur J Neurosci. 2006; 24:750–760. [PubMed: 16930405]

18. Seigneur E, Sudhof TC. Cerebellins are differentially expressed in selective subsets of neurons throughout the brain. J Comp Neurol. 2017; 525:3286–3311. [PubMed: 28714144]

19. Krishnan V, et al. Autism gene Ube3a and seizures impair sociability by repressing VTA Cbln1. Nature. 2017; 543:507–512. [PubMed: 28297715]

20. Seigneur E, Polepalli JS, Sudhof TC. Cbln2 and Cbln4 are expressed in distinct medial habenula-interpeduncular projections and contribute to different behavioral outputs. Proc Natl Acad Sci U S A. 2018; 115:E10235–E10244. [PubMed: 30287486]

21. Seigneur E, Sudhof TC. Genetic ablation of all cerebellins reveals synapse organizer functions in multiple regions throughout the brain. J Neurosci. 2018; 38:4774–4790. [PubMed: 29691328]

22. Tao W, Diaz-Alonso J, Sheng N, Nicoll RA. Postsynaptic delta1 glutamate receptor assembles and maintains hippocampal synapses via Cbln2 and neurexin. Proc Natl Acad Sci U S A. 2018; 115:E5373–E5381. [PubMed: 29784783]

23. Favuzzi E, et al. Distinct molecular programs regulate synapse specificity in cortical inhibitory circuits. Science. 2019; 363:413–417. [PubMed: 30679375]

24. Fossati M, et al. Trans-synaptic signaling through the glutamate receptor Delta-1 mediates inhibitory synapse formation in cortical pyramidal neurons. Neuron. 2019; 104:1081–1094 e1087. [PubMed: 31704028]

25. Yuzaki M, Aricescu AR. A GluD coming-of-age story. Trends Neurosci. 2017; 40:138–150. [PubMed: 28110935]

26. Kakegawa W, et al. Anterograde C1ql1 signaling is required in order to determine and maintain a single-winner climbing fiber in the mouse cerebellum. Neuron. 2015; 85:316–329. [PubMed: 25611509]

27. Sigoillot SM, et al. The secreted protein C1ql1 and its receptor BAI3 control the synaptic connectivity of excitatory inputs converging on cerebellar purkinje cells. Cell Rep. 2015; 10:820–832. [PubMed: 25660030]

28. Martinelli DC, et al. Expression of C1ql3 in discrete neuronal populations controls efferent synapse numbers and diverse behaviors. Neuron. 2016; 91:1034–1051. [PubMed: 27478018]

29. Matsuda K, et al. Transsynaptic modulation of kainate receptor functions by C1q-like proteins. Neuron. 2016; 90:752–767. [PubMed: 27133466]

30. Straub C, et al. Distinct subunit domains govern synaptic stability and specificity of the kainate receptor. Cell Rep. 2016; 16:531–544. [PubMed: 27346345]

31. Schwenk J, et al. High-resolution proteomics unravel architecture and molecular diversity of native AMPA receptor complexes. Neuron. 2012; 74:621–633. [PubMed: 22632720]

32. Loh KH, et al. Proteomic analysis of unbounded cellular compartments: synaptic clefts. Cell. 2016; 166:1295–1307 e1221. [PubMed: 27565350]

33. Xu D, et al. Narp and NP1 form heterocomplexes that function in developmental and activity-dependent synaptic plasticity. Neuron. 2003; 39:513–528. [PubMed: 12895424]

34. O'Brien RJ, et al. Synaptic clustering of AMPA receptors by the extracellular immediate-early gene product Narp. Neuron. 1999; 23:309–323. [PubMed: 10399937]

35. Sia GM, et al. Interaction of the N-terminal domain of the AMPA receptor GluR4 subunit with the neuronal pentraxin NP1 mediates GluR4 synaptic recruitment. Neuron. 2007; 55:87–102. [PubMed: 17610819]

36. Lee SJ, et al. Presynaptic neuronal pentraxin receptor organizes excitatory and inhibitory synapses. J Neurosci. 2017; 37:1062–1080. [PubMed: 27986928]

37. Farhy-Tselnicker I, et al. Astrocyte-secreted glypican 4 regulates release of neuronal pentraxin 1 from axons to induce functional synapse formation. Neuron. 2017; 96:428–445 e413. [PubMed: 29024665]

38. Chang MC, et al. Narp regulates homeostatic scaling of excitatory synapses on parvalbumin-expressing interneurons. Nat Neurosci. 2010; 13:1090–1097. [PubMed: 20729843]

39. Pelkey KA, et al. Pentraxins coordinate excitatory synapse maturation and circuit integration of parvalbumin interneurons. Neuron. 2015; 85:1257–1272. [PubMed: 25754824]

40. Trotter JH, et al. Synaptic neurexin-1 assembles into dynamically regulated active zone nanoclusters. J Cell Biol. 2019; 218:2677–2698. [PubMed: 31262725]

41. Biederer T, Kaeser PS, Blanpied TA. Transcellular nanoalignment of synaptic function. Neuron. 2017; 96:680–696. [PubMed: 29096080]

42. Srinivasan N, et al. Comparative analyses of pentraxins: implications for protomer assembly and ligand binding. Structure. 1994; 2:1017–1027. [PubMed: 7881902]

43. Iijima T, Iijima Y, Witte H, Scheiffele P. Neuronal cell type-specific alternative splicing is regulated by the KH domain protein SLM1. J Cell Biol. 2014; 204:331–342. [PubMed: 24469635]

44. Masugi-Tokita M, Shigemoto R. High-resolution quantitative visualization of glutamate and GABA receptors at central synapses. Curr Opin Neurobiol. 2007; 17:387–393. [PubMed: 17499496]

45. Oakley H, et al. Intraneuronal beta-amyloid aggregates, neurodegeneration, and neuron loss in transgenic mice with five familial Alzheimer's disease mutations: potential factors in amyloid plaque formation. J Neurosci. 2006; 26:10129–10140. [PubMed: 17021169]

46. Gotz J, Bodea LG, Goedert M. Rodent models for Alzheimer disease. Nat Rev Neurosci. 2018; 19:583–598. [PubMed: 30194347]

47. Crouzin N, et al. Area-specific alterations of synaptic plasticity in the 5XFAD mouse model of Alzheimer's disease: dissociation between somatosensory cortex and hippocampus. PLoS One. 2013; 8:e74667. [PubMed: 24069328]

48. Asboth L, et al. Cortico-reticulo-spinal circuit reorganization enables functional recovery after severe spinal cord contusion. Nat Neurosci. 2018; 21:576–588. [PubMed: 29556028]

49. Chen B, et al. Reactivation of dormant relay pathways in injured spinal cord by KCC2 manipulations. Cell. 2018; 174:521–535 e513. [PubMed: 30033363]

50. Sathyamurthy A, et al. Massively parallel single nucleus transcriptional profiling defines spinal cord neurons and their activity during behavior. Cell Rep. 2018; 22:2216–2225. [PubMed: 29466745]

51. Aoto J, Martinelli DC, Malenka RC, Tabuchi K, Sudhof TC. Presynaptic neurexin-3 alternative splicing trans-synaptically controls postsynaptic AMPA receptor trafficking. Cell. 2013; 154:75–88. [PubMed: 23827676]

52. Bradbury EJ, et al. Chondroitinase ABC promotes functional recovery after spinal cord injury. Nature. 2002; 416:636–640. [PubMed: 11948352]

53. Basso DM, et al. Basso Mouse Scale for locomotion detects differences in recovery after spinal cord injury in five common mouse strains. J Neurotrauma. 2006; 23:635–659. [PubMed: 16689667]

54. Cheng CH, et al. Local delivery of high-dose chondroitinase ABC in the sub-acute stage promotes axonal outgrowth and functional recovery after complete spinal cord transection. PLoS One. 2015; 10:e0138705. [PubMed: 26393921]

55. Ferrer-Ferrer M, Dityatev A. Shaping synapses by the neural extracellular matrix. Front Neuroanat. 2018; 12:40. [PubMed: 29867379]

56. Diering GH, Huganir RL. The AMPA receptor code of synaptic plasticity. Neuron. 2018; 100:314–329. [PubMed: 30359599]

57. Fukata Y, et al. Epilepsy-related ligand/receptor complex LGI1 and ADAM22 regulate synaptic transmission. Science. 2006; 313:1792–1795. [PubMed: 16990550]

58. Lovero KL, Fukata Y, Granger AJ, Fukata M, Nicoll RA. The LGI1-ADAM22 protein complex directs synapse maturation through regulation of PSD-95 function. Proc Natl Acad Sci U S A. 2015; 112:E4129–4137. [PubMed: 26178195]

59. Laverty D, et al. Cryo-EM structure of the human alpha1beta3gamma2 GABAA receptor in a lipid bilayer. Nature. 2019; 565:516–520. [PubMed: 30602789]

60. Canitano R, Pallagrosi M. Autism spectrum disorders and schizophrenia spectrum disorders: excitation/inhibition imbalance and developmental trajectories. Front Psychiatry. 2017; 8:69. [PubMed: 28507523]

61. Aricescu AR, Lu W, Jones EY. A time- and cost-efficient system for high-level protein production in mammalian cells. Acta Crystallogr D Biol Crystallogr. 2006; 62:1243–1250. [PubMed: 17001101]

62. Harbury PB, Zhang T, Kim PS, Alber T. A switch between two-, three-, and four-stranded coiled coils in GCN4 leucine zipper mutants. Science. 1993; 262:1401–1407. [PubMed: 8248779]

63. Elegheert J, et al. Lentiviral transduction of mammalian cells for fast, scalable and high-level production of soluble and membrane proteins. Nat Protoc. 2018; 13:2991–3017. [PubMed: 30455477]

64. Takeo YH, Kakegawa W, Miura E, Yuzaki M. RORalpha regulates multiple aspects of dendrite development in cerebellar Purkinje cells *in vivo*. J Neurosci. 2015; 35:12518–12534. [PubMed: 26354918]

65. Walter TS, et al. A procedure for setting up high-throughput nanolitre crystallization experiments. Crystallization workflow for initial screening, automated storage, imaging and optimization. Acta Crystallogr D Biol Crystallogr. 2005; 61:651–657. [PubMed: 15930615]

66. Winter G, Lobley CM, Prince SM. Decision making in xia2. Acta Crystallogr D Biol Crystallogr. 2013; 69:1260–1273. [PubMed: 23793152]

67. Sauter NK, Grosse-Kunstleve RW, Adams PD. Robust indexing for automatic data collection. J Appl Crystallogr. 2004; 37:399–409. [PubMed: 20090869]

68. Evans P. Scaling and assessment of data quality. Acta Crystallogr D Biol Crystallogr. 2006; 62:72–82. [PubMed: 16369096]

69. Evans PR. An introduction to data reduction: space-group determination, scaling and intensity statistics. Acta Crystallogr D Biol Crystallogr. 2011; 67:282–292. [PubMed: 21460446]

70. Kabsch W. Integration, scaling, space-group assignment and post-refinement. Acta Crystallogr D Biol Crystallogr. 2010; 66:133–144. [PubMed: 20124693]

71. McCoy AJ, et al. Phaser crystallographic software. J Appl Crystallogr. 2007; 40:658–674. [PubMed: 19461840]

72. Murshudov GN, et al. REFMAC5 for the refinement of macromolecular crystal structures. Acta Crystallogr D Biol Crystallogr. 2011; 67:355–367. [PubMed: 21460454]

73. Adams PD, et al. PHENIX: a comprehensive Python-based system for macromolecular structure solution. Acta Crystallogr D Biol Crystallogr. 2010; 66:213–221. [PubMed: 20124702]

74. Langer G, Cohen SX, Lamzin VS, Perrakis A. Automated macromolecular model building for X-ray crystallography using ARP/wARP version 7. Nat Protoc. 2008; 3:1171–1179. [PubMed: 18600222]

75. Emsley P, Lohkamp B, Scott WG, Cowtan K. Features and development of Coot. Acta Crystallogr D Biol Crystallogr. 2010; 66:486–501. [PubMed: 20383002]

76. Chen VB, et al. MolProbity: all-atom structure validation for macromolecular crystallography. Acta Crystallogr D Biol Crystallogr. 2010; 66:12–21. [PubMed: 20057044]

77. The PyMOL Molecular Graphics System, Version 1.7. Schrödinger; LLC:

78. Howarth M, et al. Monovalent, reduced-size quantum dots for imaging receptors on living cells. Nat Methods. 2008; 5:397–399. [PubMed: 18425138]

79. Myszka DG. Improving biosensor analysis. J Mol Recognit. 1999; 12:279–284. [PubMed: 10556875]

80. Chen Y, et al. NS21: re-defined and modified supplement B27 for neuronal cultures. J Neurosci Methods. 2008; 171:239–247. [PubMed: 18471889]

81. Schindelin J, et al. Fiji: an open-source platform for biological-image analysis. Nat Methods. 2012; 9:676–682. [PubMed: 22743772]

82. Pavlov I, et al. Tonic GABAA conductance bidirectionally controls interneuron firing pattern and synchronization in the CA3 hippocampal network. Proc Natl Acad Sci U S A. 2014; 111:504–509. [PubMed: 24344272]

83. Nikonenko AG, et al. Enhanced perisomatic inhibition and impaired long-term potentiation in the CA1 region of juvenile CHL1-deficient mice. Eur J Neurosci. 2006; 23:1839–1852. [PubMed: 16623841]

84. Kakegawa W, et al. Differential regulation of synaptic plasticity and cerebellar motor learning by the C-terminal PDZ-binding motif of GluRdelta2. J Neurosci. 2008; 28:1460–1468. [PubMed: 18256267]

85. Franklin SL, Love S, Greene JR, Betmouni S. Loss of perineuronal net in ME7 prion disease. J Neuropathol Exp Neurol. 2008; 67:189–199. [PubMed: 18344910]

86. Senkov O, et al. Polysialylated neural cell adhesion molecule is involved in induction of long-term potentiation and memory acquisition and consolidation in a fear-conditioning paradigm. J Neurosci. 2006; 26:10888–109898. [PubMed: 17050727]

87. Senkov O, Mironov A, Dityatev A. A novel versatile hybrid infusion-multielectrode recording (HIME) system for acute drug delivery and multisite acquisition of neuronal activity in freely moving mice. Front Neurosci. 2015; 9:425. [PubMed: 26594144]

88. Minge D, et al. Heparan sulfates support pyramidal cell excitability, synaptic plasticity, and context discrimination. Cereb Cortex. 2017; 27:903–918. [PubMed: 28119345]

89. Saito T. *In vivo* electroporation in the embryonic mouse central nervous system. Nat Protoc. 2006; 1:1552–1558. [PubMed: 17406448]

90. Takeuchi K, et al. Chondroitin sulphate N-acetylgalactosaminyl-transferase-1 inhibits recovery from neural injury. Nat Commun. 2013; 4:2740. [PubMed: 24220492]

One Sentence Summary

Structural biology information was used to design CPTX, a synthetic protein that induces functional excitatory synapses and restores normal behaviors in mouse models of neurological diseases.
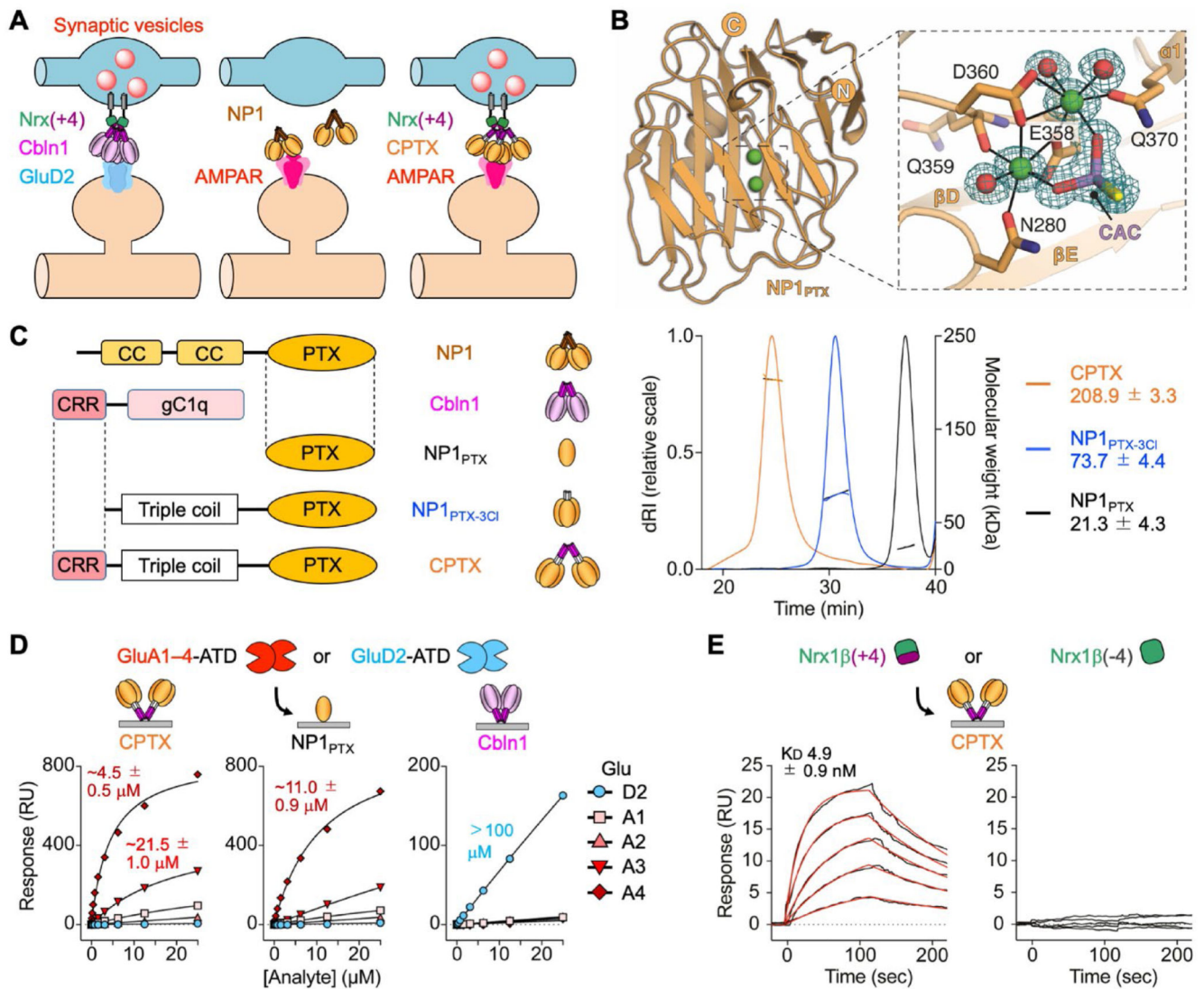
Fig. 1. Structure-guided design and biophysical characterization of CPTX.
(**A**) The CPTX concept. While Cbln1 induces synapse formation by binding to postsynaptic GluD2 and presynaptic Nrx(+4), NP1 induces clustering of postsynaptic AMPARs without inducing presynaptic elements. CPTX is a chimeric ESP consisting of Cbln1 and NP1 structural elements. (**B**) Crystal structure of the pentraxin domain of human NP1 (NP1$_{PTX}$). The N- and C-termini are annotated. Calcium ions (Ca^{2+}) and water molecules are shown as green and red spheres, respectively. 2mFo-DFc electron density is contoured at 1.0 σ. The Ca^{2+} coordination shell, which includes a cacodylate buffer molecule (CAC), is indicated by black lines. (**C**) Diagrams of CPTX and related constructs. CC, coiled-coil domain; PTX, pentraxin domain; CRR, cysteine-rich region; gC1q, globular C1q domain; 3Cl, triple coil. The graph on the right shows molecular masses of monomeric NP1$_{PTX}$, trimeric NP1$_{PTX-3Cl}$ and hexameric CPTX. dRI, differential refractive index. (**D**) Binding isotherms for the interactions between the GluA1–4 or GluD2 ATDs and immobilized CPTX, NP1$_{PTX}$ and Cbln1. The GluA4 ATD interacted strongest with CPTX (K_D ~ 4.5 ± 0.5 μM) and NP1$_{PTX}$

($K_D \sim 11.0 \pm 0.9$ μM), but not with Cbln1. In contrast, the ATD of GluD2 only interacted with Cbln1 ($K_D > 100$ μM). (**E**) Single-cycle kinetic sensorgrams for the interaction between the ectodomain of Nrx1β(±4) and immobilized CPTX. CPTX directly bound to Nrx1β(+4) ($K_D \sim 4.90 \pm 0.90$ nM), but not to Nrx1β(–4).
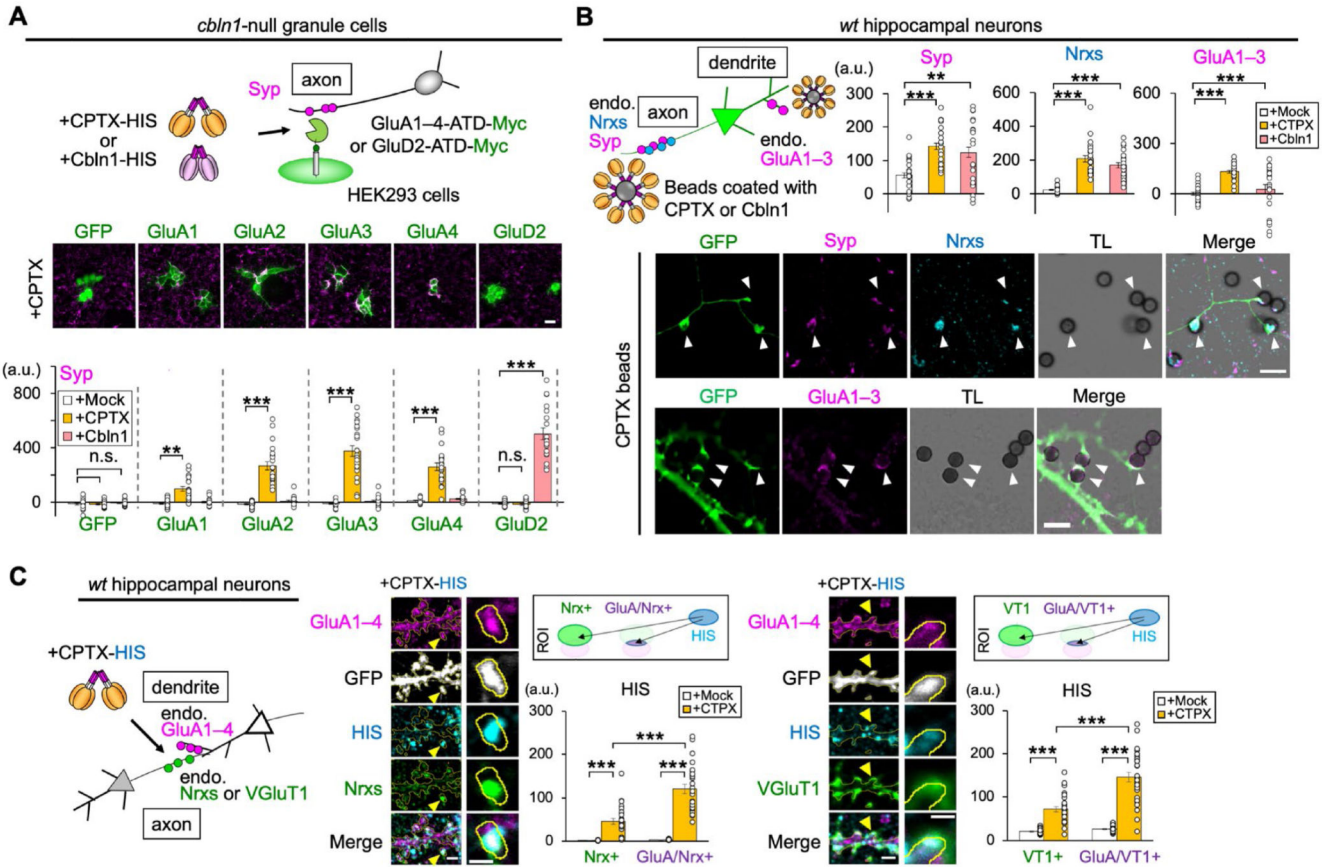
Fig. 2. CPTX directly induces excitatory pre- and postsynaptic sites in vitro.
(**A**) CPTX induced the accumulation of presynaptic terminals of cerebellar granule cells onto co-cultured HEK293 cells displaying AMPAR ATDs. The intensities of the synaptophysin immunoreactivity (Syp; magenta) onto HEK293 cells (green) are quantified in the lower graph. Mock, vehicle (HEPES buffered saline (HBS)) controls. The bars represent the mean ± SEM. ***$P < 0.001$, **$P < 0.01$, $n = 16$–22 fields from 7 independent experiments, one-way ANOVA followed by Tukey's test. Scale bar, 20 μm. (**B**) Beads coated with CPTX induced the formation of presynaptic boutons positive for endogenous synaptophysin (Syp) and neurexins (Nrxs), and postsynaptic boutons positive for GluA1–3, in co-cultured hippocampal neurons transfected with GFP. Arrowheads indicate beads immuno-positive for Syp (magenta, middle panel), Nrxs (cyan) or GluA1–3 (magenta, lower panel). Mock, beads coated with anti-HIS antibody. TL, transmitted light. Scale bar, 5 μm. The intensities of the Syp, Nrxs and GluA1–3 immunoreactivity onto beads are quantified in the upper graphs. The bars represent the mean ± SEM. ***$P < 0.001$, **$P < 0.01$, $n = 21$ fields from 5 experiments, one-way ANOVA followed by Tukey's test. (**C**) CPTX localizes at excitatory synapses. Representative immunocytochemical staining images show Nrxs or VGluT1 (green), GluA1–4 (magenta) and HIS-tagged CPTX (cyan) in hippocampal neurons. Dendritic spines indicated by yellow arrowheads are magnified. Mean intensities of HIS signals in the Nrx-positive (Nrx+) or VGluT1-positive (VT1+) areas were measured and compared to those in the areas overlapping with GluA1–3 signals (GluA/Nrx+ or GluA/

VT1+). The bars represent the mean ± SEM. ***$P < 0.001$, $n = 24$–26 fields from 2–3 independent experiments, Student's t-test with Bonferroni correction. Scale bars, 2 μm (left panels), 1 μm (magnifications).
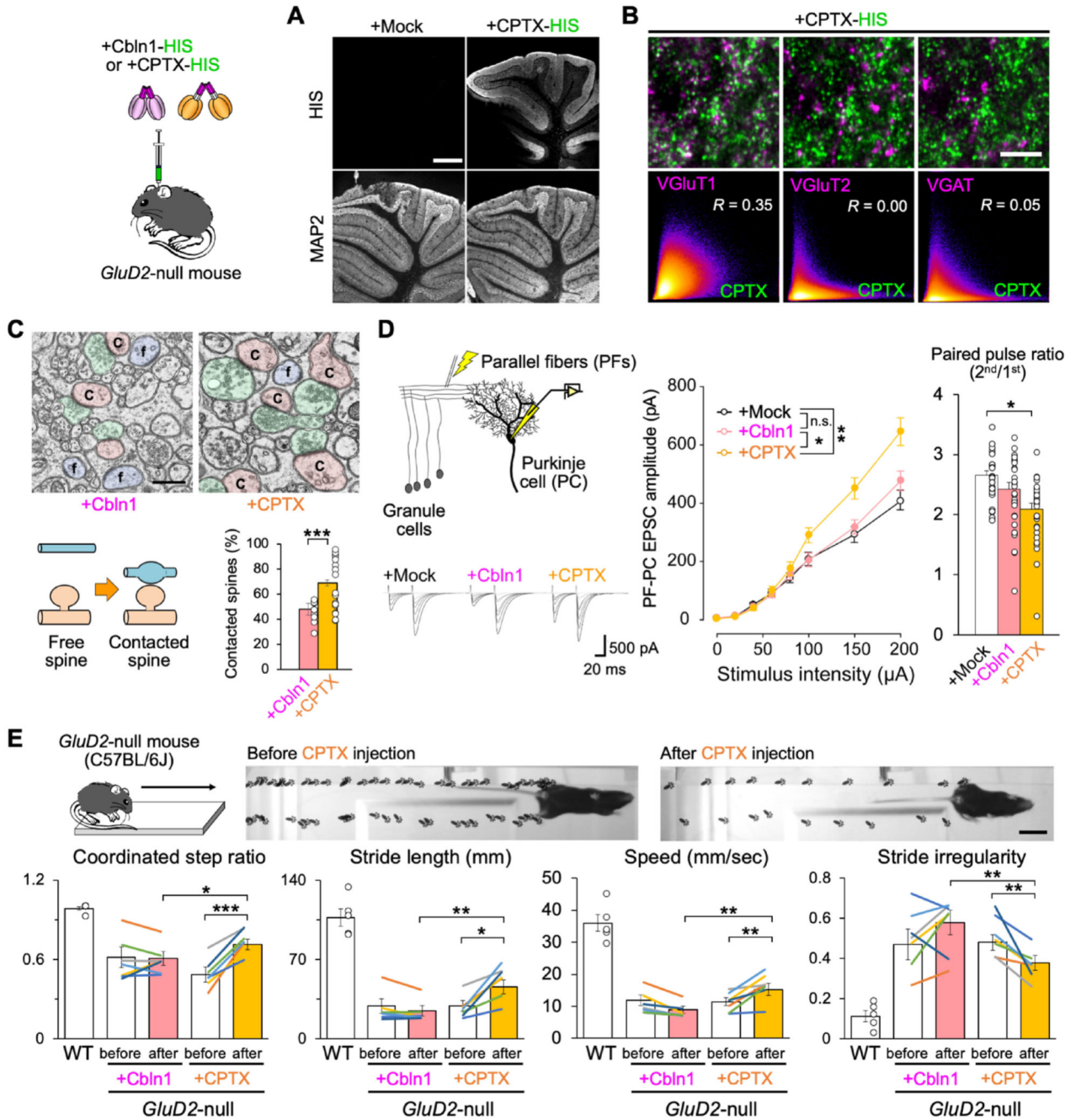
Fig. 3. CPTX restores PF-PC synapses and motor coordination in *GluD2*-null mice.
(**A**) HIS-tagged CPTX injected into the *GluD2*-null cerebellum localizes at PF–PC synapses. Mock, vehicle. Scale bar, 500 μm. (**B**) HIS immunoreactivity in the molecular layer of the injected area (A) colocalized with VGluT1 (a PF marker), but not VGluT2 (a climbing fiber marker) or VGAT (an inhibitory input marker). The scatter plots show the 2D pixel intensity histograms for CPTX (green) and each synapse marker (magenta). Pearson's correlation coefficient *R* values are indicated. Scale bar, 2 μm. (**C**) Representative electron microscopic images show free dendritic spines (f, blue) and contacted spines (c, red) innervated by PFs

(green) in the *GluD2*-null cerebellum 3 d after injection of Cbln1 or CPTX. Scale bar, 500 nm. The fractions of contacted PC spines are quantified in the lower graph. ***P* < 0.001, *n* = 10–20 sections from 1–2 mice, χ^2 test. (**D**) CPTX restores functional PF–EPSCs in *GluD2*-null mice 3 d after injection. Representative traces are shown. The middle graph shows averaged input-output relationships of PF–EPSCs for each treatment. **P < 0.01, *P < 0.05, n.s. not significant, *n* = 30 cells each, two-way ANOVA followed by Scheffe *post-hoc* test. The right graph shows the paired-pulse ratio of the 2nd to 1st PF–EPSC amplitudes. *P < 0.05, *n* = 30 cells each, Kruskal-Wallis test followed by Scheffe *post-hoc* test. (**E**) CPTX improves the gait of *GluD2*-null mice 3 d after the injection. Representative footprints before and after CPTX injection are shown near the top. The lower graphs show the quantification of gait parameters. Each line represents an individual score before and after injection with either Cbln1 or CPTX. ***P < 0.001, **P < 0.01, *P < 0.05, *n* = 5–6 mice, Student's (paired) *t*-test. Scale bar, 50 mm. The bars represent the mean ± SEM. (**C**–**E**).
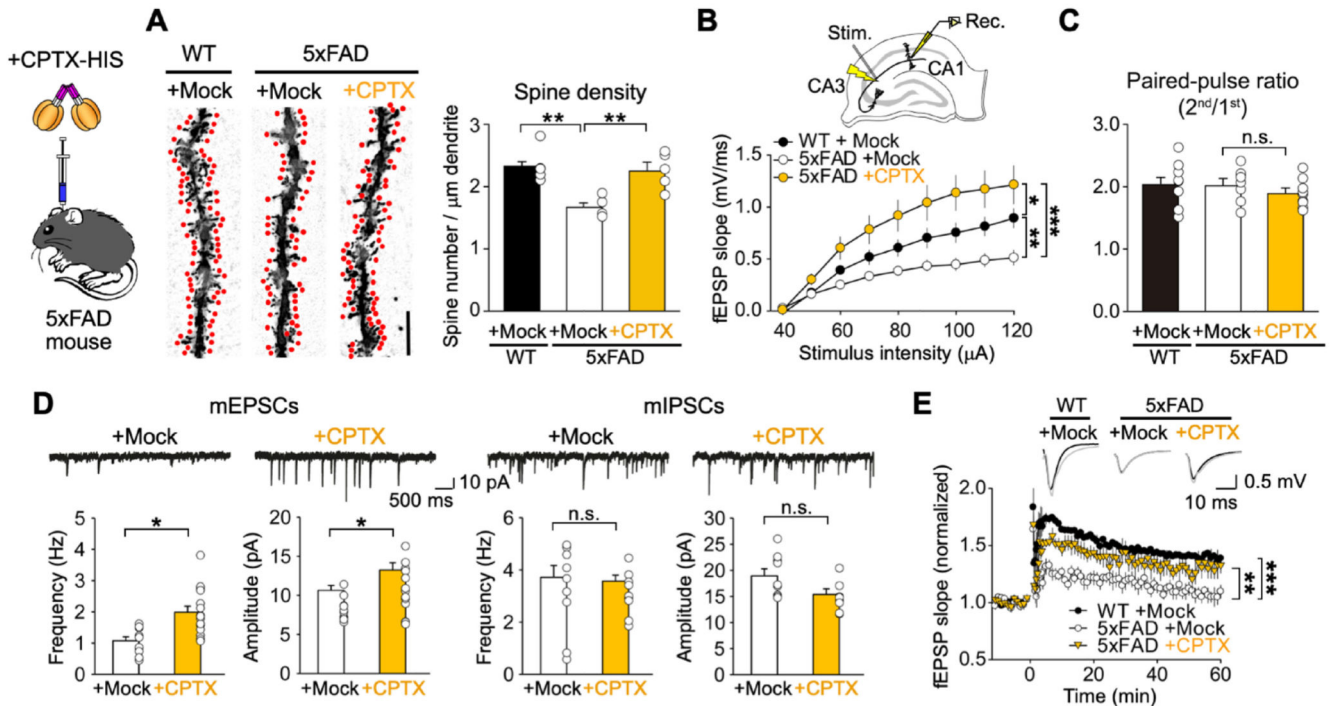
Fig. 4. CPTX restores spines and LTP in the hippocampus of an Alzheimer's disease model.
(**A**) CPTX restores dendritic spine density in 5xFAD mice. Representative Golgi-Cox staining of apical dendrites of CA1 pyramidal neurons in the dorsal hippocampus. Red marks indicate counted spines. Mock, vehicle (HBS buffer) controls. Scale bar, 5 μm. The graph shows the averaged spine density for 7–8 secondary apical dendrites for each animal. The bars represent the mean ± SEM. $**P < 0.01$, $n = 4$–5 mice, one-way ANOVA followed by Holm-Sidak *post-hoc* test. (**B**) CPTX restores Schaffer collateral (SC)-evoked field excitatory postsynaptic potentials (fEPSPs) in 5xFAD mice. The graph shows averaged input-output relationships of SC–fEPSPs for each treatment. Mock, vehicle (HBS buffer) controls. The bars represent the mean ± SEM. $***P < 0.001$, $**P < 0.01$, $*P < 0.05$, $n = 6$–9 slices, repeated two-way ANOVA. (**C**) CPTX does not affect the presynaptic release probability. The graph shows the paired-pulse ratio of the 2nd to 1st SC-fEPSP amplitudes at 50-ms intervals. The bars represent the mean ± SEM. n.s. not significant, $n = 8$–9 slices, Student's *t*-test. (**D**) CPTX increases the frequency and the amplitude of mEPSCs, but not mIPSCs, in the 5xFAD hippocampus. Representative traces are shown near the top. $**P < 0.01$, $*P < 0.05$, $n = 9$–15 cells, Student's *t*-test. (**E**) CPTX restores LTP in 5xFAD mice. Application of theta-burst stimulation to SC three times induced a robust LTP at SC-CA1 synapses in the mock-treated WT, but not in the mock-treated 5xFAD hippocampus. Representative SC-fEPSP traces are shown. The bars represent the mean ± SEM. $***P < 0.001$, $**P < 0.01$, $n = 8$–9 slices, one-way ANOVA on ranks followed by Holm-Sidak *post-hoc* test for the mean values from the last 15 min of the recording.
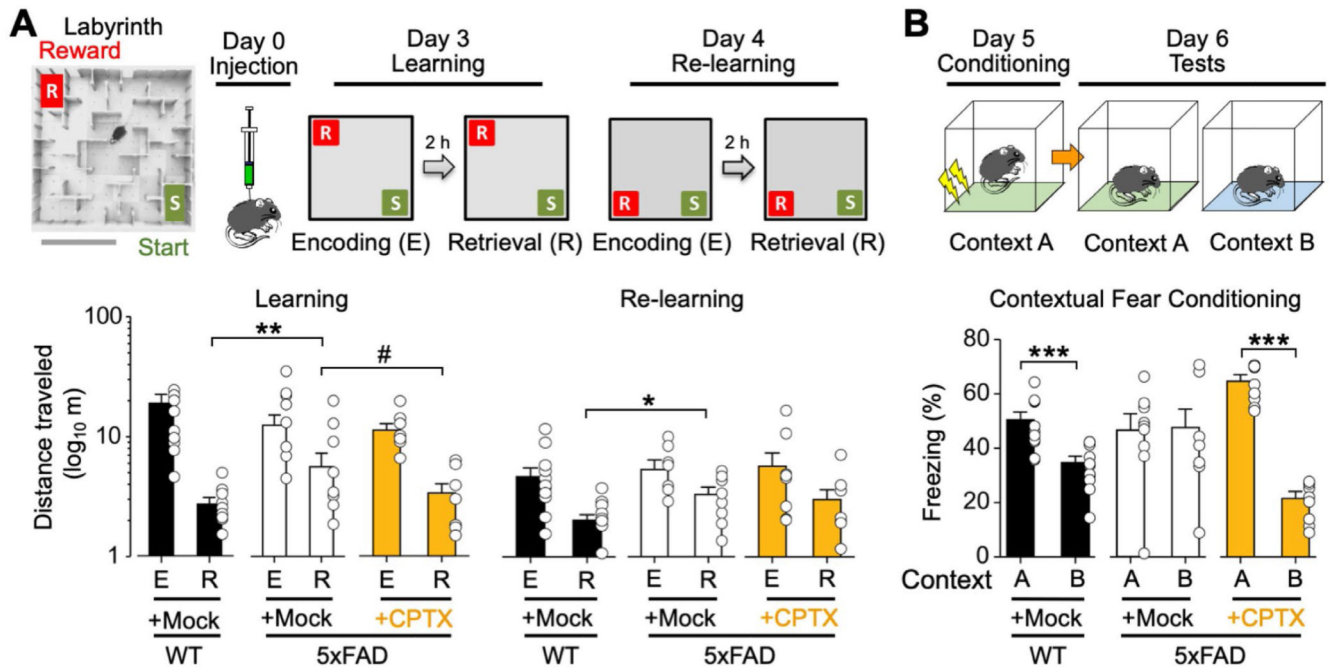
Fig. 5. CPTX restores hippocampus-dependent behaviors in an Alzheimer's disease model.
(**A**) CPTX improves spatial memory in 5xFAD mice. CPTX or Mock (vehicle) was injected in 5xFAD mice on day 0. On day 3, mice were placed at the start point (S) of a 3D-printed maze and the pellet was placed at the reward point (R). Two hours after the initial encoding (E) session, mice were returned to the same start point to examine memory integrity in the retrieval (R) session. On the next day, the position of reward was changed, and reversal learning (re-learning) was evaluated. Scale bar, 30 cm. The averaged total distances that mice traveled to reach the goal during the encoding and the retrieval sessions are shown in the lower graph. Log_{10} scaling of the y-axis facilitates comparison of distances before and after training. The bars represent the mean ± SEM. **$P < 0.01$, *$P < 0.05$, #$P < 0.1$, $n = 8$–11 mice, two-way repeated measures ANOVA followed by Fisher's *post-hoc* Least Significant Difference (LSD) test. (**B**) CPTX restores context discrimination in 5xFAD mice. CPTX or Mock (vehicle) was injected in 5xFAD mice on day 0. Electrical shock was applied to wild-type and 5xFAD mice in context A on day 5. Freezing time was measured in context A and context B on day 6. The lower graph shows the mean (± SEM) freezing time of each group. ***$P < 0.001$, $n = 8$–11 mice, Student's paired *t*-test.
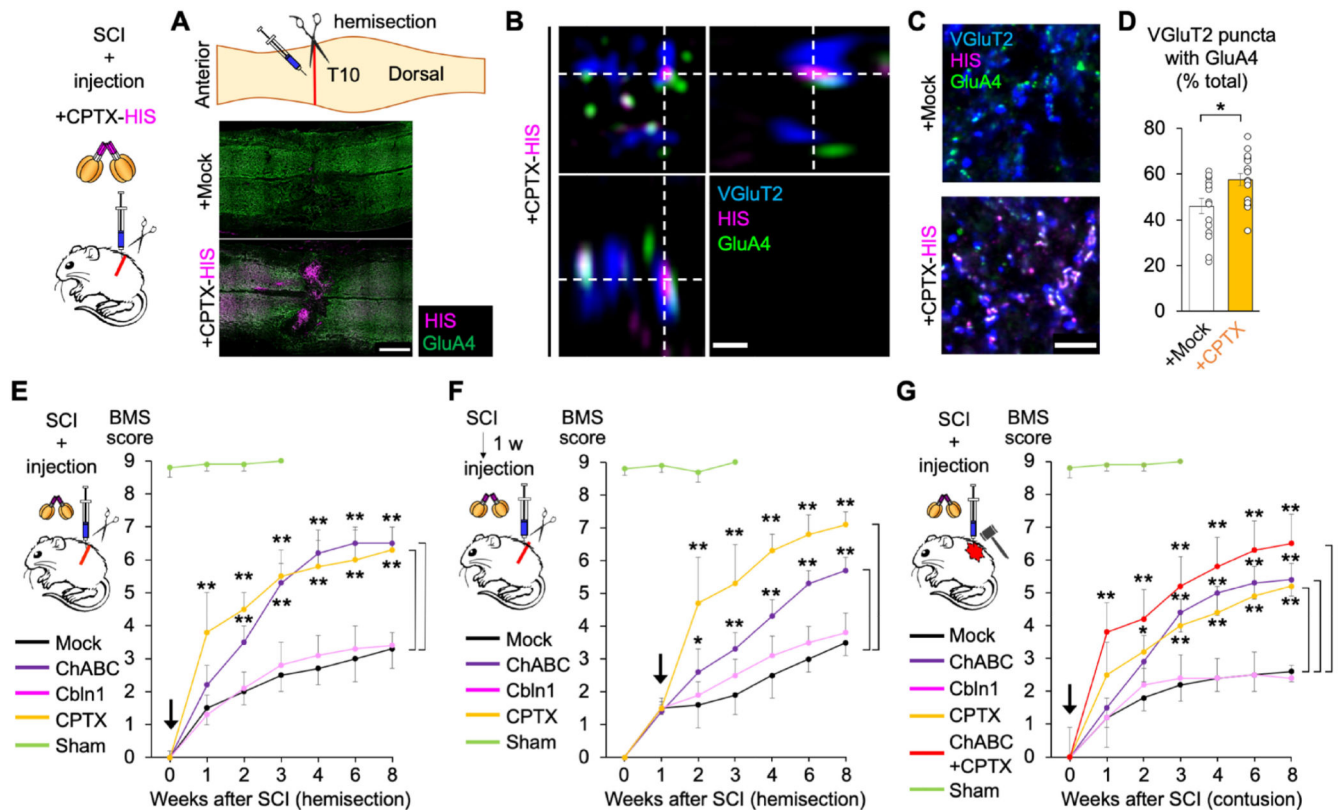
Fig. 6. CPTX promotes restoration of synapses and motor function in spinal cord injury.
(**A**) Schematic depiction of SCI caused by hemisection at the 10th thoracic vertebra (T10). The lower panels show representative horizontal sections of the spinal cord immunostained for VGluT2, HIS (CPTX) and GluA4 upon Mock (vehicle) or CPTX injection. Scale bar, 0.5 mm. (**B**) Representative orthogonal images obtained by Airyscan super-resolution microscopy indicating the localization of CPTX in proximity of VGluT2- and GluA4-immunopositive puncta. Scale bar, 0.5 μm. (**C**) Representative immunohistochemical staining images of coronal sections stained for VGluT2 (blue), GluA4 (green) and HIS (CPTX; magenta) from mock- or CPTX-treated spinal cords. Scale bar, 5 μm. (**D**) Quantification of the fraction of GluA4+/VGluT2+-double-positive puncta. The bars represent the mean ± SEM. *$P < 0.05$, $n = 16$ slices from 8 mice, Student's t-test. (**E–G**) Time-course analyses of locomotion (Basso Mouse Scale (BMS) score) in SCI mice after injections. Mock (vehicle), Chondroitinase ABC (ChABC), Cbln1 or CTPX were injected into the spinal cord immediately (**E**) or 1 week after (**F**) hemisection, or immediately after contusion by impactors (**G**, 70 kdyn impact force). For the sham controls, the spinal cord was surgically exposed without imposing injury or injection. Mice that showed a BMS score of 1.5 at 1 week after hemisection were selected for **F**. **$P < 0.01$, *$P < 0.05$, $n = 9$ mice for each treatment, repeated two-way ANOVA with *post-hoc* Bonferroni-Dunn test (comparing the various treatments with Mock for each time point).